Editors' Suggestion

Inspiral-merger-ringdown waveforms with gravitational self-force results within the effective-one-body formalism

Benjamin Leather,[1] Alessandra Buonanno,[1,2] and Maarten van de Meent[3,1]

[1]*Max Planck Institute for Gravitational Physics (Albert Einstein Institute), Am Mühlenberg 1, Potsdam 14476, Germany*

[2]*Department of Physics, University of Maryland, College Park, Maryland 20742, USA*

[3]*Center of Gravity, Niels Bohr Institute, Blegdamsvej 17, 2100 Copenhagen, Denmark*

(Received 23 May 2025; accepted 25 June 2025; published 7 August 2025)

Gravitational self-force (GSF) theory is a strong-gravity perturbative approach to the relativistic two-body problem, primarily developed to model extreme-mass-ratio inspirals, where one compact object is significantly more massive than the companion. However, recent advancements in GSF calculations, particularly involving second-order self-force (2GSF) results, indicated a much broader applicability across a wider range of mass ratios. These developments have motivated efforts to incorporate GSF results into the effective-one-body (EOB) framework, where they have already been successfully integrated into the state-of-the-art waveform model, `SEOBNRV5`, employed in recent LIGO-Virgo-KAGRA observing runs. In this work, we present `SEOBNR-GSF`, a nonspinning inspiral-merger-ringdown (IMR) EOB waveform model that introduces a GSF-informed EOB Hamiltonian as its central innovation. This marks the first complete IMR waveform model constructed primarily from GSF results. We show that our model outperforms inspiral waveforms from full 2GSF calculations in the intermediate-to-comparable mass regime. Furthermore, by comparing with a post-Newtonian-informed variant, `SEOBNR-GSF-PN`, we demonstrate that the inclusion of numerical GSF information in the Hamiltonian leads to significant improvements in model fidelity. Finally, we benchmark our model against high-accuracy, nonspinning numerical-relativity simulations from the Simulating eXtreme Spacetimes (SXS) catalog and find that its median mismatch is comparable to that of `SEOBNRV5`, suggesting that this approach holds promise for further enhancing future EOB waveform models.

DOI: 10.1103/6qc3-xn17

I. INTRODUCTION

The growth of gravitational-wave astronomy since the first observation of a binary black-hole (BH) merger in 2015 [1] is indebted to accurate theoretical descriptions of the two-body dynamics and gravitational radiation in general relativity (GR). The extension in frequency bandwith and diversity of astrophysical sources from current and future detectors requires continual improvement in waveform models. From a modeling perspective, this improvement rests in the symbiosis of numerical and analytical methods. Numerical relativity (NR) [2–4], the fully nonlinear realization of the two-body problem in GR, produces the most accurate waveforms, but remains computationally expensive for practical waveform generation. This necessitates the development of approximate models for waveform production that are sufficiently efficient, yet do not compromise on accuracy to support the science goals of upcoming gravitational wave (GW) observatories.

Three main perturbative frameworks underpin such approximate modelling schemes: post-Newtonian (PN) theory [5–17], valid in the weak-field, small-velocity regime $v^2/c^2 \sim GM/rc^2 \ll 1$[1]; post-Minkowskian (PM) theory [18–26], applicable in the weak fields whereby $GM/rc^2 \ll 1$, but allowing relativistic velocities $v^2/c^2 \leq 1$; and gravitational self-force (GSF) theory, which captures strong-field dynamics in the small mass-ratio limit, $q = m_2/m_1 \ll 1$. While each of these frameworks provides crucial insights into different aspects of the two-body problem's dynamics, none can, on its own, accurately model the complete evolution of a binary across the entire parameter space. The integration of these methods would allow for a more comprehensive and precise description

[1]Here $M = m_1 + m_2$ is the total mass of system, where m_1 and m_2 are masses of the primary and secondary, respectively. r is the radial separation.

Published by the American Physical Society under the terms of the Creative Commons Attribution 4.0 International license. Further distribution of this work must maintain attribution to the author(s) and the published article's title, journal citation, and DOI. Open access publication funded by the Max Planck Society.

of the waveform throughout all phases of a binary's evolution.

For ground-based detectors, three primary methods have been developed to construct complete waveform models that span the entire parameter space of compact binaries: NR surrogate models, phenomenological models, and effective-one-body (EOB) models. Surrogate models [27–33] interpolate between NR simulations using dimensionality reduction techniques, achieving high accuracy but limited in parameter space coverage and waveform duration. Phenomenological models [34–43] fit closed-form expressions to hybrid PN/EOB-NR waveforms, enabling fast waveform generation across broad parameter ranges, but relying on NR and EOB for calibration. EOB formalism [44–49] combines insights from two-body methods to provide a comprehensive description of compact binary dynamics. EOB resums information from two-body methods in such a way as to include the exact strong-field test-particle limit. More precisely, EOB maps the dynamics of a binary system to that of a test body of a deformed background spacetime, with the deformation being parametrized by the symmetric mass ratio, ν. Being a physical approach, it has the advantage that not only the waveforms, but multiple observables (e.g., binding energy, periastron advance, scattering angle) can be compared to NR, assessing its consistency and robusteness. On the other side, since EOB waveforms are built in time-domain, solving ordinary differential equations makes the waveform generation slower than when using closed-form, frequency-domain waveforms, but they are more accurate since fewer approximations are adopted. Currently, two main families of EOB waveform models exist: SEOBNR (see Refs. [50–54]), which will be the focus of this work and, TEOBRESUMS (see Refs. [55–59]).

Effective-one-body and phenomenological models form the backbone of waveform modelling used by the LIGO-Virgo-Kagra (LVK) Collaboration [60–70]. EOB models have traditionally relied on sophisticated resummations of the PN expansion. However, the upcoming generation of GW observatories—including next-generation (XG) ground-based detectors like the Einstein Telescope [71] and Cosmic Explorer [72,73], as well as the space-based laser interferometer space antenna mission [74]—is expected to significantly extend the accessible parameter space and increase signal-to-noise ratios by up to two orders of magnitude [75]. This makes the need for more accurate and robust waveform models increasingly urgent. Recent work, such as Refs. [76,77], has shown that even state-of-the-art waveform models may induce significant biases when applied to future LVK and XG signals, particularly in regimes with large mass ratios or high BH spins.

To address the need for enhanced waveform accuracy, recent efforts have focused on developing new methods for on incorporating perturbative results beyond PN into the EOB framework. Notably, recent work in Ref. [78] has integrated PM information into the SEOBNR framework, resulting in a novel IMR waveform model, `SEOBNR-PM`. This model is built upon a PM-expanded Hamiltonian, utilizing an expansion in GM/rc^2, as opposed to the traditional PN expansion in v^2/c^2. However, PN information is also included, where necessary. Preliminary comparisons indicate that `SEOBNR-PM` demonstrates promising performance relative to the current state-of-the-art `SEOBNRV5` model, even achieving superior agreement with NR during the inspiral phase before calibration to NR.

An equally promising direction lies in the incorporation of GSF results, which provide precise information in the strong-field, small mass-ratio regime. GSF theory naturally complements the EOB framework, since in the test-particle limit, the EOB dynamics reduce to the motion in a fixed background. Furthermore, GSF calculations distinguish between conservative (time-symmetric) and dissipative (time-antisymmetric) components of the dynamics, which aligns well with the EOB formulation. Recent advances have enabled the computation of second-order GSF (2GSF) quantities, including gravitational wave fluxes [79] and binding energies [80], and the construction of the first postadiabatic waveforms for quasicircular, nonspinning binaries [81].

To date, GSF information has primarily been incorporated into EOB models to improve the radiation-reaction sector, including fluxes and mode amplitudes, through calibration in the test-particle limit [52]. The only conservative input so far has been the innermost stable circular orbit (ISCO) shift from first-order GSF calculations [82]. Attempts to inform the EOB Hamiltonian using GSF data face significant obstacles: most notably, the appearance of gauge singularities at the light ring when evolving in the standard EOB gauge [83,84]. While an alternative gauge developed in Refs. [84,85] has been proposed to avoid this pathology, it has not yet been incorporated into a full IMR EOB model.

The structure of this paper is as follows. In Sec. II, we review the necessary elements of the EOB theory that are critical for constructing a GSF-informed EOB Hamiltonian. This includes a discussion of the light-ring gauge singularity in the standard EOB gauge and the alternative gauge proposed in Refs. [84,85] to mitigate this issue. Section. III introduces a post-Schwarzschild gauge Hamiltonian with corrections up to 4PN order, which extends the results of Antonelli *et al.* [84] by including higher-order terms. Following this, Sec. IV examines the SEOBNR framework, with a focus on incorporating our new Hamiltonian into a full IMR waveform model. In Sec. V, we outline the calibration of the model against NR simulations. Section VI presents a detailed comparison of the model's performance against `SEOBNRV5`, assessing the agreement of the binding energy and waveforms relative to 2GSF (1PAT1) ones, and computing mismatches with NR data. Finally, Sec. VII concludes with a summary of our findings and a discussion of future research directions.

A. Notation

We shall first introduce some conventions that are used throughout. We use geometrized units such that $G = c = 1$ and adopt the metric signature $(-+++)$. For an exemplar binary with masses m_1 and m_2, with $m_1 \geq m_2$, we define the *reduced mass* to be $\mu \coloneqq m_1 m_2/M$, where $M \coloneqq m_1 + m_2$ is the total mass of the system. Another important quantity is the *symmetric mass ratio*, $\nu \coloneqq \mu/M$. In the binary's center of mass, the EOB dynamics is described by $q_a \coloneqq (r, \varphi)$, with canonically conjugate momenta $p_a \coloneqq (p_r, p_\varphi)$. In practice, we often use the mass-reduced inverse orbital separation, $u \coloneqq M/r$, and the mass-reduced momenta $\hat{p}_r \coloneqq p_r/\mu$ and $\hat{p}_\varphi \coloneqq p_\varphi/\mu$. Similarly, any Hamiltonian written with a "hat" is the mass-reduced version such that $\hat{H} \coloneqq H/\mu$.

II. EFFECTIVE-ONE-BODY THEORY

In (nonspinning) EOB, the motion of the inspiralling binary system is mapped to that of a test mass in a deformed Schwarzschild spacetime. The connection between the real Hamiltonian, $H_{\rm EOB}$, and the effective Hamiltonian, $H_{\rm eff}$ is given by the energy map:

$$H_{\rm EOB} = M\sqrt{1 + 2\nu\left(\frac{H_{\rm eff}}{\mu} - 1\right)}. \tag{1}$$

The EOB effective metric associated with this effective Hamiltonian has a line element of the form

$$g^{\rm eff}_{\mu\nu}dx^\mu dx^\nu = -A(r,\nu)dt^2 + [A(r,\nu)\bar{D}(r,\nu)]^{-1}dr^2 + r^2 d\Omega^2 \tag{2}$$

together with the *mass-shell condition* [46,85],

$$g^{\mu\nu}_{\rm eff}p_\mu p_\nu + \mu^2 + Q(u,\nu,p_r,p_\varphi) = 0. \tag{3}$$

We have introduced the nongeodesic function, $Q(u,\nu,p_r,p_\varphi)$, in order to preserve the mapping in Eq. (2) through 3PN-order [84]. The generic form of the effective Hamiltonian, $H_{\rm eff}$, is then found through the simple relation, $H_{\rm eff} = -p_0$, yielding

$$H^2_{\rm eff} = A(u,\nu)[\mu^2 + A(u,\nu)\bar{D}(r,\nu)p_r^2 + p_\varphi^2 u^2 + Q(u,\nu,p_r,p_\varphi)]. \tag{4}$$

In the test mass limit, whereby $\nu \to 0$, the potentials $A(u,\nu)$ and $\bar{D}(u,\nu)$ reduce to

$$A(u,\nu)|_{\nu\to 0} = 1 - 2u, \qquad \bar{D}(u,\nu)|_{\nu\to 0} = 1, \tag{5}$$

and hence we retain the usual Schwarzschild Hamiltonian given by

$$\hat{H}^2_{\rm S} = (1-2u)[1 + (1-2u)p_r^2 + p_\varphi^2 u^2]. \tag{6}$$

$A(u,\nu)$, $\bar{D}(u,\nu)$, and $Q(u,\nu,p_r,p_\varphi)$ are fixed by writing a particular ansatz for the potentials within the Hamiltonian expression for Eq. (4), then matching this Hamiltonian through some gauge invariant quantity or through a canonical transformation to a PN-informed Hamiltonian.

Traditionally, EOB waveforms developed for observations in the LVK Collaboration use in Eq. (4) a polynomial structure of the potentials almost entirely informed by PN information. For example, the $A(u,\nu)$ potential has the simple form in the nonspinning case,

$$A(u,\nu) = 1 - 2u + A_2(\nu)u^2 + A_3(\nu)u^3 + A_4(\nu)u^4 + \mathcal{O}(u^5 \ln u). \tag{7}$$

In fact, this form becomes even simpler than Eq. (7) initially suggests, since the 1PN coefficient, $A_2(\nu)$, vanishes, whilst the coefficients $A_3(\nu)$ and $A_4(\nu)$ (i.e. up to 3PN) remain linear in ν. The potentials, $A(u,\nu)$, $\bar{D}(u,\nu)$, and $Q(u,\nu,p_r,p_\varphi)$, are known to 5.5PN order [86], but are missing two quadratic-in-ν coefficients in $A(u,\nu)$ and $\bar{D}(u,\nu)$ at 5PN.

In general, the potential $Q(u,\nu,p_r,p_\varphi)$ allows one to augment the EOB Hamiltonian through 3PN order, ensuring the original mapping outlined in Eq. (1) remains unmodified. Furthermore, the mass-reduced potential $\hat{Q}(u,\nu,\hat{p}_r,\hat{p}_\varphi)$ variably incorporates the mass-reduced radial and angular momenta, *a priori*. Henceforth, we shall denote the $\hat{Q}$ function that only depends on the radial momentum as $\hat{Q}^{\rm DJS}(u,\nu,\hat{p}_r)$, after the initials of the three authors of Ref. [46] who first used it. It should be noted, however, that this freedom need not be fixed in this way and other choices of this $\hat{Q}$ potential can be made (see, e.g., Refs. [87,88]). Fixing this freedom means the reduced angular momentum only appears as $\sim\hat{p}_\varphi^2 u^2$ and not explicitly within any of the potentials $A(u,\nu)$, $\bar{D}(u,\nu)$, and $\hat{Q}^{\rm DJS}(u,\nu,\hat{p}_r)$.

It was also shown in Ref. [46] that $\hat{Q}^{\rm DJS}(u,\nu,\hat{p}_r)$ has the form,

$$\hat{Q}^{\rm DJS}(u,\nu,\hat{p}_r) = \hat{p}_r^4 q_4(u) + \hat{p}_r^6 q_6(u) + \mathcal{O}(\hat{p}_r^8), \tag{8}$$

such that this mass-shell deformation term vanishes quartically[2] in the limit of $\hat{p}_r \to 0$. Therefore, within the Damour, Jaranowski, and Schaefer (DJS) gauge, one is forced to incorporate the p_φ^2 term into the geodesic part of the Hamiltonian.

[2]As in Ref. [46], this can be seen by generalizing the pseudo EOB "Hamilton-Jacobi" equation and comparing it to Eq. (3): $\mu^2 + g^{\mu\nu}_{\rm eff}p_\mu p_\nu + A^{\mu\nu\gamma\delta}p_\mu p_\nu p_\gamma p_\delta + \ldots = 0$.

In the DJS gauge, the EOB-potentials can be rexpressed as a GSF-inspired expansion in the mass-ratio, ν, at fixed u, whilst the form of the expansions appearing in Eqs. (7) and (8) correspond to that of PN, (i.e., an expansion in u for fixed ν). If we again consider the potentials $A(u,\nu), Q^{\rm DJS}(u,\nu,p_r), \bar{D}(u,\nu)$, we have linear-in-$\nu$ expansions about the Schwarzschild (nonspinning) limit,

$$A(u,\nu) = 1 - 2u + \nu a(u) + \mathcal{O}(\nu^2), \tag{9a}$$

$$\bar{D}(u,\nu) = 1 + \nu \bar{d}(u) + \mathcal{O}(\nu^2), \tag{9b}$$

$$Q^{\rm DJS}(u,\nu,p_r) = \nu q(u) p_r^4 + \mathcal{O}(\nu^2). \tag{9c}$$

In particular if we focus on the first of these expanded potentials, Eq. (9), it has been shown the function $a(u)$ can be directly related to the linear-in-ν correction to the gauge-invariant quantity known as the *Detweiler redshift* [83,89–95].

The Detweiler redshift can be understood most simply from a self-force (SF) perspective. In this description, the comparatively smaller secondary is considered to be a perturbation of the background (Schwarzschild) geometry such that the secondary moves on a geodesic of the effective (GSF) metric $\tilde{g}_{\mu\nu} = g_{\mu\nu} + h^R_{\mu\nu}$. The eponymous redshift variable is defined as

$$z \coloneqq (\tilde{u}^t)^{-1} \frac{d\tilde{\tau}}{dt}, \tag{10}$$

where $\tilde{u}^\alpha$ is the four-velocity Normalized in the effective metric, $\tilde{g}_{\mu\nu}$, to linear-order in ν: $\tilde{g}_{\mu\nu}\tilde{u}^\mu\tilde{u}^\nu = -1 + \mathcal{O}(\nu)$. Here t and $\tilde{\tau}$ are the coordinate time and proper time in the effective metric, respectively. It is important to stress that since the Detweiler redshift is calculated in the effective metric, this quantity cannot be interpreted as the physical gravitational redshift. A more physical interpretation is that z is proportional to the surface gravity[3] of the smaller BH's horizon [96,97].

One can decompose z to extract the linear-in-ν correction to the redshift,

$$z(x) = \sqrt{1-3x} + \nu \Delta z(x) + \mathcal{O}(\nu^2), \tag{11}$$

where $\Delta z(x)$ (at fixed x) can be expressed as

$$\Delta z(x) = \frac{x}{\sqrt{1-3x}} - \frac{1}{2}\sqrt{1-3x} h^R_{uu}(x). \tag{12}$$

Here we have introduced the notation $h^R_{uu} \coloneqq h^R_{\mu\nu}u^\mu u^\nu$, which is simply the double contraction of the regular metric perturbation with the four-velocity. Furthermore x is the gauge-independent frequency parameter, defined as $x \coloneqq (M\Omega)^{2/3}$ where Ω is the orbital frequency. It is important to note here that in SF calculations, the expansion of the redshift is viewed as an expansion in the (small) mass-ratio $q = m_2/m_1$ at fixed dimensionless frequency parameter $y = (m_1\Omega)^{2/3}$. The equivalent expansion in the context of SF to Eq. (11) is

$$z(y) = \sqrt{1-3y} + q\Delta z^{\rm 1SF}(y) + \mathcal{O}(q^2). \tag{13}$$

Although similar, the different form of the expansion in Eq. (11), as powers of ν instead of q, whilst holding x fixed instead of y, means that the expansion coefficients differ even at linear-order in q. Since y and x are related through q and ν, one finds

$$\Delta z(x) = \Delta z^{\rm 1SF}(x) + \frac{x}{\sqrt{1-3x}}, \tag{14}$$

through $\mathcal{O}(q)$.

Since this expression does not involve any derivatives of the (regular) metric perturbation and, as first noted in [89], is somewhat a gauge-invariant quantity, then this makes the redshift extremely appealing for use in synergistic studies with EOB. Another feature of the Detweiler redshift is that one can relate Δz to the linear-in-ν correction to the $A(u,\nu)$ potential through the *first law of binary-black-hole mechanics* [92,98] such that

$$a(x) = \Delta z(x)\sqrt{1-3x} - x\left(1 + \frac{1-4x}{\sqrt{1-3x}}\right). \tag{15}$$

One should note that this relation is expressed in terms of the gauge-independent x, to align this with the rest of the section, rather the usual EOB inverse radius, u, which is gauge dependent. However, the two expressions are trivially related since up to linear order in ν: $x = u + \mathcal{O}(\nu)$.

A. Divergence at the light ring in DJS gauge

As first observed in Ref. [83], attempts to use the Detweiler redshift to inform the EOB potential, $a(x)$, encounter divergences toward the light ring (LR), as $x \to 1/3$. This is obvious from the last term in Eq. (15) when we approach the LR, i.e. as $x \to 1/3$. This divergence, however, is not limited to the form of the expression for $a(x)$. As was first observed in Ref. [83] and in subsequent numerical SF codes, the contracted metric perturbation does indeed diverge at the light ring.

Firstly, let us consider the divergence of the SF quantity, h^R_{uu}. This was shown to diverge as $h^R_{uu} \sim E_{\rm S}(x)^3$ as $x \to 1/3$, where $E_{\rm S}(x)$ is the specific energy of a particle in Schwarzschild spacetime,

[3]This relationship can be shown to be exact up to linear-order in the mass-ratio through the approach of matched asymptotic expansions [96] and has been confirmed numerically through NR simulations [97].

$$E_{\rm S}(x) = \frac{1-2x}{\sqrt{1-3x}}. \tag{16}$$

As shown in Ref. [83] (and further supported in Ref. [99]), the origin of this divergence can be traced to a simple heuristic argument: the metric perturbation is sourced not only by the rest mass m_2 of the secondary, but by its conserved energy, $m_2 E_{\rm S}(x)$. Accordingly, $h^R_{\mu\nu} \sim E_{\rm S}(x)$ near the LR and the contraction with the particle's four-velocity, whose u^0 component also scales as $E_{\rm S}(x)$, leads to the cubic divergence observed in h^R_{uu}.

The second divergence appearing in Eq. (12) is manifest as the $(1-3x)^{-1/2}$ factor that appears in the bracketed term. At first glance, this behavior might suggest the presence of a physical singularity in the EOB formalism. However, as shown in Ref. [83], the divergence is analogous to the coordinate singularity in Schwarzschild spacetime and does not reflect any physical pathology. More precisely, the singular behavior of the potential, $a(u)$, near the light ring is a consequence of the choice of standard phase space coordinates used in the DJS gauge. Reference [83] showed that this divergence can be removed entirely by performing a suitable simpletic transformation, which amounts to a change of phase-space variables. Therefore, to develop an EOB Hamiltonian informed by SF, it appears essential to entirely forsake the conventional DJS gauge in favor of a gauge more suitable for the resummation of SF data.

B. Post-Schwarzschild gauge

In light of the divergences appearing in the DJS gauge, an alternative prescription initially suggested in Ref. [83] and further detailed in Ref. [85] proposes relaxing the gauge conditions of the DJS gauge. This modification allows the $\hat{Q}$ potential to scale as $\hat{Q} \sim \hat{p}_\varphi^3$ in the limit $\hat{p}_\varphi \to \infty$ and $\hat{p}_r \to 0$. In this modification to the usual gauge fixing, one fixes the radial metric coefficient in Eq. (2) to be equal to the Schwarzschild metric. The corrections to the test-mass limit (TML) of the effective Hamiltonian are then incorporated into the $\hat{Q}$ potential such that

$$\hat{H}^{\rm PS}_{\rm eff} = \sqrt{\hat{H}^2_{\rm S} + (1-2u)\hat{Q}^{\rm PS}(u, \hat{H}_{\rm S}, \nu)}. \tag{17}$$

As in [84,100], we shall refer to this alternative gauge as a *post-Schwarzschild (PS) gauge*.

In such a family of Hamiltonians, the information encapsulating the dynamics of the binary inspiral are now included inside the $\hat{Q}^{\rm PS}$-potential, rather than the usual $\hat{A}^{\rm DJS}$ potential. Moreover, the $\hat{Q}^{\rm PS}$ potential in the PS Hamiltonian has a generic functional dependence on $\hat{H}_{\rm S}$. One can therefore capture the divergent behavior toward the LR through a leading-order cubic term in $\hat{H}_{\rm S}$, as was first indicated in Ref. [85].

The $\hat{Q}^{\rm PS}$ potential can also be expressed analytically through 3PM + 4PN order as

$$\begin{aligned}\hat{Q}^{\rm PS}_{\rm 3PM+4PN} = {} & u^2 q_{\rm 2PM}(\hat{H}_{\rm S}, \nu) + u^3 q_{\rm 3PM}(\hat{H}_{\rm S}, \nu) \\ & + \Delta_{\rm 3PN}(u, \hat{H}_{\rm S}, \nu) + \Delta_{\rm 4PN}(u, \hat{H}_{\rm S}, \nu) + \mathcal{O}(5{\rm PN}),\end{aligned} \tag{18}$$

where we include up to 4PN correction terms. The coefficients, $q_{\rm nPM}$, up to 3PM order are determined from calculation of the scattering angle [85,100]. The higher-order PN correction terms, expressed as expansions in the PN parameters u and $\hat{H}^2_{\rm S} - 1$, are added as complimentary information to the purely PM expansions to ensure a match to the standard EOB DJS Hamiltonian up to 4PN order [101]. To determine these terms, one takes the 4PN expansion of the 3PM Hamiltonian in Eq. (18) and performs a canonical transformation. Then, the Hamiltonians are matched to the known 4PN EOB Hamiltonian in the DJS gauge, allowing one to solve for the unknown coefficients: $\Delta_{\rm 3PN}(u, \hat{H}_{\rm S}, \nu)$ and $\Delta_{\rm 4PN}(u, \hat{H}_{\rm S}, \nu)$. This information shall become important when considering augmenting the SF informed EOB Hamiltonian beyond linear order in the mass ratio.

The concept of a redshift-informed potential, denoted as $\hat{Q}^{\rm PS}_{\rm SF}$,[4] and its subsequent implementation into a PS gauge Hamiltonian that seamlessly incorporates SF information without resulting in a divergence at the LR, was first introduced by Antonelli *et al.* in Ref. [84]. In this work, a PS gauge Hamiltonian was constructed from fitting regularized redshift data up from SF calculations up to the LR, but in such a manner that it remained analytic beyond it. This Hamiltonian was then supplemented by incorporating additional PN information from the analytical expression of the $\hat{Q}^{\rm PS}$ potential in Eq. (18), thereby including beyond linear order in the mass-ratio information as well as noncircular orbit terms. In the following sections, we will briefly summarize its construction, whilst considering improvements on the original Hamiltonian. A more complete derivation, including additional corrections up to 3PN-order, can be found in the opening sections to Ref. [84].

III. POST-SCHWARZSCHILD GAUGE HAMILTONIAN WITH 4PN CORRECTIONS

A. Post-Schwarzschild gauge Hamiltonian informed from self-force

We shall consider the same ansatz for our $\hat{Q}^{\rm PS}_{\rm SF}$-potential as Ref. [84],

[4]The potential, $\hat{Q}^{\rm PS}_{\rm SF}$, informed by Δz data, was originally labeled as $\hat{Q}^{\rm PS}_{\rm SMR}$, with "SMR" signifying "small-mass-ratio." For greater clarity and to more accurately reflect its association with SF effects, we have adopted "SF" in place of "SMR," hence the notation $\hat{Q}^{\rm PS}_{\rm SF}$.

$$\hat{Q}^{\rm PS}_{\rm SF}(u,\hat{H}_{\rm S},\nu)=\nu[f_0(u)\hat{H}_{\rm S}^5+f_1(u)\hat{H}_{\rm S}^2+f_2(u)\hat{H}_{\rm S}^3\ln\hat{H}_{\rm S}^{-2}]. \tag{19}$$

The first term, proportional to $\hat{H}_{\rm S}^5$, is designed to capture the global divergence that appears in the redshift. As stated previously (see also footnote in Ref. [84]), a leading term proportional to $\hat{H}_{\rm S}^3$ would be sufficient to modify the divergence of $\sim(1-3x)^{-3/2}$, but this leads to pathological eccentriclike behavior toward the LR. Therefore, we make the same minimal correction as Ref. [84] that remedies this behavior, whilst still capturing the divergence. The second and third terms, proportional to $\sim(1-3x)^{-1/2}$ and $\sim\ln(1-3x)^{1/2}$, respectively, incorporate the problematic subleading terms appearing in the redshift and would potentially spoil the behavior of the Hamiltonian toward the LR.

To fix the functions $f_i(u)$ $(i\in1,2,3)$, one follows the procedure first outlined in Ref. [91], and subsequently followed in Ref. [84], by matching the binding energy from the EOB Hamiltonian and from SF calculations to linear order in ν at fixed frequency. To compute the circular orbit binding energy from the PS-gauge Hamiltonian, one first determines the circular-orbit azimuthal momentum, $\hat{p}_\varphi^{\rm circ}$, by solving the Hamilton equation,

$$\dot{p}_r=-\frac{\partial H_{\rm EOB}}{\partial r}(r,p_r=0,p_\varphi,\nu)=0. \tag{20}$$

This expression for $\hat{p}_\varphi^{\rm circ}$ is then used to express the gauge-dependent inverse radius u and its gauge-dependent counterpart, x, to linear order in ν through the second Hamilton equation for the circular orbit frequency,

$$\Omega=\frac{\partial H_{\rm EOB}}{\partial p_\varphi}(r,p_r=0,p_\varphi,\nu). \tag{21}$$

The intermediate expressions for $\hat{p}_\varphi^{\rm circ}$ and $u^{\rm circ}(x,\nu)$ were given in Ref. [84] and are rewritten for completeness in Appendix A. Together, the expressions for $\hat{p}_\varphi^{\rm circ}$ and $u^{\rm circ}(x,\nu)$ allow one to compute a gauge-invariant expression for the circular-orbit Hamiltonian, $\hat{H}_{\rm EOB}(x,\nu)$, and therefore the binding energy, $\hat{E}^{\rm EOB}_{\rm bind}(x,\nu)$ via the definition,

$$\hat{E}^{\rm EOB}_{\rm bind}\coloneqq\frac{H_{\rm EOB}-M}{\mu}. \tag{22}$$

This yields an expression for the binding energy entirely in terms of x, ν, and the functions $f_i(x)$ and their derivatives to linear order in ν.

In the same circular-orbit limit, one can express the binding energy in terms of the linear-in-ν correction to the redshift, $\Delta z(x)$ [see Eq. (11)], through the first law of binary BH mechanics [98]. Explicitly, the binding energy is,

$$\hat{E}^{\rm SF}_{\rm bind}(x,\nu)=\frac{1-2x}{\sqrt{1-3x}}-1+\nu\left[\frac{\Delta z(x)}{2}+\frac{(7-24x)x}{6(1-3x)^{3/2}}-\frac{x}{3}\Delta z'(x)+\sqrt{1-3x}-1\right]+\mathcal{O}(\nu^2), \tag{23}$$

where $'$ denotes differentiation with respect to x. Once one has the two binding energies, it is possible to link the redshift correction appearing in Eq. (23) to the $\hat{Q}^{\rm PS}_{\rm SF}$ potential through the functions $f_i(u)$. In order to do this within an EOB model, one needs to produce a suitable analytical fit for the correction to the redshift, Δz. Furthermore, as noted previously, one needs to be careful of the actual divergent behavior of the SF results for the Detweiler redshift. Thus, Ref. [84] decomposes $\Delta z(x)$ further to anticipate the form of the fit to high-precision-numerical SF results such that

$$\Delta z(x)=\frac{\Delta z^{(0)}(x)}{1-3x}+\frac{\Delta z^{(1)}(x)}{\sqrt{1-3x}}+\frac{\Delta z^{(2)}(x)}{1-3x}\ln E_{\rm S}^{-2}(x). \tag{24}$$

The functions, $\Delta z^{(i)}(x)$, $(i\in0,1,2)$ are the actual pieces fitted to the numerical redshift data, whilst at the same time remaining analytic so as to preserve the analytic nature of the EOB model beyond the LR. To ensure these functions enter the potential in such a way to preserve the analyticity of the PS-gauge Hamiltonian, we separate the functions $f_i(x)$ with the ansatz,

$$f_i(x)=\tilde{f}_i(x)+\sum_{j=0}^{j=2}f_i^{(j)}(x)\Delta z^{(j)}(x),\qquad i\in0,1,2. \tag{25}$$

By imposing smoothness at the LR, by which we mean they should be free of spurious terms like $(1-3x)^{-1/2}$ or $\ln E_{\rm S}^{-2}$, we obtain solutions for the coefficients $\tilde{f}_i(x)$ and $f_i^{(j)}(x)$, with the rest of the function determined by the form of the fit to the redshift. The nonzero solutions, given first in Ref. [84], read

$$\tilde{f}_0(x)=-\frac{x(1-3x)(1-4x)}{(1-2x)^5}, \tag{26a}$$

$$\tilde{f}_1(x)=-\frac{x}{(1-2x)^2}, \tag{26b}$$

$$f_0^{(0)}(x)=\frac{1-3x}{(1-2x)^5}, \tag{26c}$$

$$f_1^{(1)}(x)=\frac{1}{(1-2x)^2}, \tag{26d}$$

$$f_2^{(2)}(x)=\frac{1}{(1-2x)^3}. \tag{26e}$$

Let us now return to the remaining part of the functions entering the PS-gauge Hamiltonian, the redshift fitting functions $\Delta z^{(i)}(x)$. There are two main considerations one must consider in the numerical fitting of these functions: (i) encoding the precise numerical information from redshift data without including the divergence at the LR, and (ii) the lack of numerical SF data beyond the LR. With this in mind, we follow the fitting procedure first outlined in the Appendix of Ref. [84] to obtain a robust and appropriate fit by utilizing a 21.5 PN expansion of Δz, first obtained in Kavanagh *et al.* in Ref. [95]. The analytical nature of this expression allows one to minimize the need for a large number of fitting parameters, as well as allowing the numerical data to be mostly responsible for augmenting the fit in the strong-field regime.

The fit takes the same form as outlined in Ref. [84], but we find it clearer to be more explicit by writing it in the following manner:

$$\Delta z = Z_0(x) + 2x^3 \frac{(1-2x)^3}{1-3x} Z_{\rm PN}(x)[1+\alpha(x) Z_{\rm fit}(x)], \tag{27}$$

where $Z_0(x)$ is the leading term that is fixed such that the leading terms $\tilde{f}_0(x)$ and $\tilde{f}_1(x)$ in Eqs. (26a) and (26b) are exactly cancelled and do not enter into the final Hamiltonian. The additional function, $\alpha(x)$, that multiples $Z_{\rm fit}$ in Eq. (27), is an attenuation function designed to ensure that in the weak field the entire fitting is dominated by the form of the high-order PN resummation, $Z_{\rm PN}(x)$, which we will discuss shortly. It is preferable, since this function inevitably enters into the expression for the Hamiltonian, that it is smooth and differentiable throughout the entire domain, and hence this is realized by taking this form to be an exponential such that

$$\alpha(x) = \exp\left[\frac{4-x^{-2}}{6}\right]. \tag{28}$$

We define $Z_{\rm PN}(x)$ by starting from the 21.5PN expression for Δz, as given in Ref. [95], setting $Z_{\rm fit}(x) = 0$ in order to analytically solve for $Z_{\rm PN}(x)$. Once inverted, the solution is re-expanded in terms of x (and $\log x$) to the same PN order as the starting series. To ensure the Hamiltonian remains finite at the horizon (i.e., $x = 1/2$), we pull out the divergent factor $(1-2x)^2$ and resum the remaining series so that $Z_{\rm PN}(x) \to 0$ as $x \to 1/2$. Omitting the full expression for the sake of brevity, the final resummed form reads

$$Z_{\rm PN}(x) = (1-2x)^2 \sum_{i,j} b_{(i,j)} x^{i/2} \log^j x, \tag{29}$$

where the first few nonzero coefficients are given by

$$b_{(0,0)} = 1, \tag{30a}$$

$$b_{(2,0)} = \frac{1}{192}(4640 - 123\pi^2), \tag{30b}$$

$$b_{(4,0)} = \frac{2126}{15} + \frac{64\gamma_{\rm E}}{5} - \frac{3301\pi^2}{1024} + \frac{128\log 2}{5}, \tag{30c}$$

$$b_{(4,1)} = \frac{32}{5}. \tag{30d}$$

Here, $\gamma_{\rm E} \simeq 0.5772$ is the Euler's constant. The final piece of the fitting function, namely $Z_{\rm fit}(x)$, is a combination of five polynomial and logarithmic terms given by,

$$Z_{\rm fit}(x) = c_0 + c_1\beta + c_2\beta^4 + (c_3\beta + c_4\beta^4)\log\left[\frac{1-3x}{(1-2x)^2}\right], \tag{31}$$

with the polynomial function $\beta := 9x(1-3x)(1-2x)$, and c_i $(i \in [0,4])$ being arbitrary coefficients to be determined by linearly fitting to numerical data. To determine the fitting coefficients c_i, Ref. [84] used the high-precision SF code developed by one of the authors in Ref. [102]. This code can be used to construct h^R_{uu} using the method of mode-sum regularization with the use of the arbitrary precision arithmetic to enable the production of high-precision results. However, as noted in Ref. [83], near the LR the precision is ultimately limited by the number of ℓ modes that are included. Due to relativistic beaming effects one needs to include order $\sim(1-3x)^{-1}\ell$ modes to achieve convergence of the mode sum for gauge invariant quantities such as the redshift towards the LR. Here, we use the same data and fitting as in [83,84], with numerical data obtained for Δz up to $(1-3x) \simeq 4\times 10^{-5}$ with 120ℓ modes. The optimal coefficients, c_i, are found to be

$$c_0 = 0.5559473282711097, \tag{32a}$$

$$c_1 = -2.5898685656267251, \tag{32b}$$

$$c_2 = 31.1449861760975693, \tag{32c}$$

$$c_3 = 2.4401152757341507, \tag{32d}$$

$$c_4 = -179.1758186033215239. \tag{32e}$$

One can then combine all of these results together to obtain the final expressions, $f_i(x)$, that enter into the $\hat{Q}^{\rm PS}_{\rm SF}$ potential, in Eq. (19). The coefficient of $H^2_{\rm S}$, $f_1(x)$, actually vanishes whilst the rest the two remaining functions can be written in the succinct form,

$$f_0(x) = \frac{1-3x}{(1-2x)^2} Z_{\rm PN}(x)[1+\alpha(x)(c_0 + c_1\beta + c_2\beta^4)], \tag{33a}$$

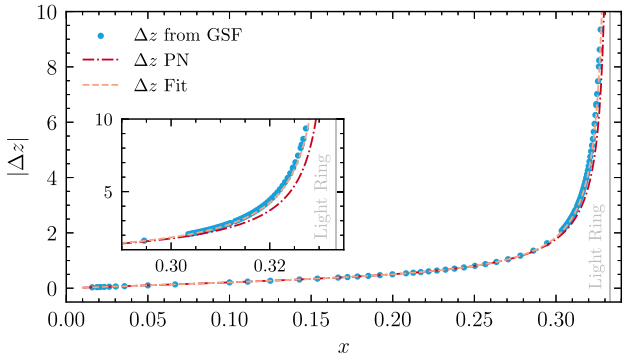


FIG. 1. We demonstrate the semianalytical fitting of the Detweiler redshift from numerical GSF data toward the LR as a function of the gauge-invariant radius, x. The raw numerical GSF data for the linear-in-ν correction to the redshift is shown by the blue circles up to $(1-3x) \simeq 4\times 10^{-5}$. Each data point has been calculated using mode-sum regularization with 120ℓ-modes. The red dash-dotted line shows the fit using only the 21.5PN expression from Ref. [95], $Z_{\rm PN}(x)$, i.e. Eq. (27) with $Z_{\rm fit}(x)$ set to 0. The orange dashed line, on the other hand, indicates the correction to the redshift as calculated using our numerical fit in conjunction with $Z_{\rm PN}(x)$ [i.e., Eq. (27) including Eq. (31)]. One can see, especially from the inset, that toward the LR the accuracy of our fit to GSF data is greatly improved by the inclusion of the fit, $Z_{\rm fit}(x)$.

$$f_2(x) = (1-2x)^2 Z_{\rm PN}(x)[1+\alpha(x)(c_3\beta + c_4\beta^4)]. \tag{33b}$$

The final semianalytical fit is demonstrated for the linear-in-ν correction to the redshift in Fig. 1.

This completes the SF-informed piece of the potential, $\hat{Q}^{\rm PS}_{\rm SF}$, but Ref. [84] showed that information beyond the circular-orbit, linear-in-mass-ratio limit can be included to enhance the $\hat{Q}^{\rm PS}$ based on previous studies of up to 4PN-order [100], see Eq. (18).

B. 3PN and 4PN corrections to the post-Schwarzschild gauge Hamiltonian

The main difficulty is that arbitrarily adding PN terms to the $\hat{Q}^{\rm PS}_{\rm SF}$ potential introduces double counting of the PN information already included implicitly into our Hamiltonian. In particular, since in the PS-gauge the momenta enters through the factors of $\hat{H}_{\rm S} = \hat{H}_{\rm S}(\hat{u}, \hat{p}_r, \hat{p}_\varphi)$, then one cannot split the potential into pieces that are purely circular and noncircular contributions. Thus, any addition of PN terms that are to linear-order-in-ν will affect the precise matching done for the binding energies for $\hat{Q}^{\rm PS}_{\rm SF}$ in the circular orbit limit. To augment the Hamiltonian further one splits the potential into a linear-order-in-ν piece, $\hat{Q}^{\rm PS}_{\rm SF}$, and then an additional term, $\Delta\hat{Q}^{\rm PS}$, informed by additional PN-terms,

$$\hat{Q}^{\rm PS}_{{\rm SF}-n{\rm PN}} = \hat{Q}^{\rm PS}_{\rm SF} + \Delta\hat{Q}^{\rm PS}_{n{\rm PN}}. \tag{34}$$

In the same manner as Ref. [84], this term has to be broken down further such that

$$\Delta\hat{Q}^{\rm PS}_{n{\rm PN}} \coloneqq \Delta\hat{Q}^{\rm PS}_{n{\rm PN(extra)}} + \Delta\hat{Q}^{\rm PS}_{n{\rm PN(count)}}, \tag{35}$$

where $\Delta\hat{Q}^{\rm PS}_{n{\rm PN(extra)}}$ captures the additional PN terms introduced up to nPN order, whilst $\Delta\hat{Q}^{\rm PS}_{n{\rm PN(count)}}$ is a counterterm designed specifically to cancel the linear-in-ν PN terms that are introduced in the first term that would spoil the agreement of the binding energy to linear-order in ν.

To calculate $\Delta\hat{Q}^{\rm PS}_{n{\rm PN(extra)}}$, we find the difference between the PN expansion of $\hat{Q}^{\rm PS}_{\rm 3PM+4PN}$ in Eq. (18) with coefficients taken from Ref. [100] and $\hat{Q}^{\rm PS}_{\rm SF}$. Given that $\hat{Q}^{\rm PS}_{\rm SF}$ is semi-analytical, incorporating SF information through fitting to numerical data rather than solely using analytical PN expressions for $\hat{Q}^{\rm PS}$, we calculate a 3PN expansion of $\hat{Q}^{\rm PS}_{\rm SF}$. This is done by replacing the numerical fitting for Δz with PN expansions of the redshift functions $\Delta z^{(i)}$, which are derived from by matching the 3PN expansion of Detweiler's redshift invariant obtained in Ref. [103] with Eq. (24). To obtain such expansions, one expands in the PN parameters u and $Y \coloneqq \hat{H}^2_{\rm S} - 1 \sim \mathcal{O}(1/c^2)$. In Ref. [84], the mixed SF-PN potential is considered up-to-3PN order, but we proceed to include the same 3PN terms *and* 4PN corrections. It is important to note there is an important distinction that $\Delta\hat{Q}^{\rm PS}_{\rm 3PN(extra)}$ is valid for generic orbits, whilst at one PN-order higher, $\Delta\hat{Q}^{\rm PS}_{\rm 4PN(extra)}$ is only valid for near-circular orbits. The 4PN tail-term corrections to the potential are only valid in the near-circular-orbit regime since the corrections are computed through an expansion in $\hat{p}_r$ up to $\mathcal{O}(\hat{p}_r^6)$, which can be thought of as an small eccentricity expansion. In this work, we utilize the 3PN and 4PN potentials, $\hat{Q}^{\rm PS}_{\rm 3PM+3PN}$ and $\hat{Q}^{\rm PS}_{\rm 3PM+4PN}$ first presented in Ref. [100], with the $\hat{Q}^{\rm PS}_{\rm 3PM+3PN}$ used in the model in Ref. [84]. The additional PN terms up to 4PN are given by,[5]

$$\Delta\hat{Q}^{\rm PS}_{\rm 3PN(extra)} = 3\nu u^2 Y + \left(3\nu - \frac{9}{4}\nu^2\right)u^2Y^2 + 3\nu u^3 + \left(22\nu - \frac{23}{4}\nu^2\right)u^3 Y + \left(16\nu - \frac{7}{2}\nu^2\right)u^4, \tag{36a}$$

[5]In Ref. [100], there is a typo in Eq. (A10). The ν^2-coefficient, $123/54\pi^2$, should read $123/64\pi^2$ as in our expression for Eq. (36b). We thank Mohammed Khalil for confirming this typographical error.

$$\begin{aligned}\Delta\hat{Q}^{\rm PS}_{\rm 4PN(extra)} &= 3u^3\nu + 3u^2Y\nu + u^3Y\left(22\nu - \frac{23\nu^2}{4}\right) + u^4\left(16\nu - \frac{7\nu^2}{2}\right) + u^2Y^2\left(3\nu - \frac{9\nu^2}{4}\right)\\ &+ u^2Y^3\left(-\frac{4135\nu}{48} - \frac{27\nu^2}{16} + \frac{15\nu^3}{8} - \frac{147432}{5}\nu\log 2 + \frac{1399437}{160}\nu\log 3 + \frac{1953125}{288}\nu\log 5\right)\\ &+ u^3Y^2\left(-\frac{304853\nu}{1200} - \frac{445\nu^2}{16} + \frac{49\nu^3}{8} - \frac{14099512}{225}\nu\log 2 + \frac{14336271}{800}\nu\log 3 + \frac{4296875}{288}\nu\log 5\right)\\ &+ u^5\left(-\frac{283739\nu}{1800} + \frac{296\gamma_{\rm E}\nu}{15} - \frac{13921\pi^2\nu}{6144}\right.\\ &\left.- \frac{2387\nu^2}{24} + \frac{205\pi^2\nu^2}{64} + \frac{9\nu^3}{4} - \frac{256216}{25}\nu\log 2 + \frac{1061181}{400}\nu\log 3 + \frac{390625}{144}\nu\log 5 + \frac{148}{15}\nu\log u\right)\\ &+ u^4Y\left(-\frac{135239\nu}{450} + \frac{296\gamma_{\rm E}\nu}{15} - \frac{13921\pi^2\nu}{6144}\right.\\ &\left.- \frac{405\nu^2}{4} + \frac{123\pi^2\nu^2}{64} + \frac{13\nu^3}{2} - \frac{9771016}{225}\nu\log 2 + \frac{1182681}{100}\nu\log 3 + \frac{390625}{36}\nu\log 5 + \frac{148}{15}\nu\log u\right). \qquad (36b)\end{aligned}$$

The second, correctional term, $\Delta\hat{Q}^{\rm PS}_{n\rm PN(count)}$, then ensures the matching done at the level of the binding energies through the redshift invariant is not disrupted by the additional PN terms in $\Delta\hat{Q}^{\rm PS}_{n\rm PN(extra)}$. To do this in a systematic way, this term is chosen to start at $(n+1)$-PN order higher than the $\Delta\hat{Q}^{\rm PS}_{n\rm PN(count)}$ term. Whereas the calculation of these particular terms is very much agnostic of the particular PN-order one is working at, the form of the counterterm, however, is different depending on the particular PN order. The main difference is that at 4PN, the counterterm must include logarithmic terms that only begin to enter $\Delta\hat{Q}^{\rm PS}_{n\rm PN(extra)}$ at 4PN-order.

At 3PN, the counterterm was first given in Ref. [84] by

$$\Delta\hat{Q}^{\rm PS}_{\rm 3PN(count)} = \nu(q^{(3,2)}_{\rm 3PN}u^3Y^2 + q^{(4,1)}_{\rm 3PN}u^4Y + q^{(5,0)}_{\rm 3PN}Y^5), \qquad (37)$$

where

$$q^{(3,2)}_{\rm 3PN} = 9, \qquad q^{(4,1)}_{\rm 3PN} = 96, \qquad q^{(5,0)}_{\rm 3PN} = 112. \qquad (38)$$

Then, at 4PN, the counterterm now starts at 5PN and now includes logarithmic terms such that

$$\Delta\hat{Q}^{\rm PS}_{\rm 4PN(count)} = \nu\sum_{i=0}^{i=3}(q^{(6-i,i)}_{\rm 4PN}u^{(6-i)}Y^i + q^{(6-i,i)}_{\rm 4PN,log}u^{(6-i)}Y^i\log u), \qquad (39)$$

where the coefficients for the nonlogarithmic terms are given by,

$$\begin{aligned}q^{(0,6)}_{\rm 4PN} &= -\frac{82139}{450} + \frac{1184\gamma_{\rm E}}{15} - \frac{13921\pi^2}{1536} - \frac{1024864\log 2}{25} + \frac{1061181\log 3}{100} + \frac{390625\log 5}{36},\\ q^{(1,5)}_{\rm 4PN} &= -\frac{92699}{120} + \frac{296\gamma_{\rm E}}{5} - \frac{13921\pi^2}{2048} - \frac{7355624\log 2}{45} + \frac{3572343\log 3}{80} + \frac{1953125\log 5}{48},\\ q^{(2,4)}_{\rm 4PN} &= -\frac{492767}{600} - \frac{16310992\log 2}{75} + \frac{25002999\log 3}{400} + \frac{7421875\log 5}{144},\\ q^{(3,3)}_{\rm 4PN} &= -\frac{4135}{16} - \frac{442296\log 2}{5} + \frac{4198311\log 3}{160} + \frac{1953125\log 5}{96}, \qquad (40)\end{aligned}$$

and the coefficients for the logarithmic terms are given by,

$$\begin{aligned}q^{(0,6)}_{\rm 4PN,log} &= \frac{592}{15}, \qquad q^{(1,5)}_{\rm 4PN,log} = \frac{148}{5},\\ q^{(2,4)}_{\rm 4PN,log} &= q^{(3,3)}_{\rm 4PN,log} = 0. \qquad (41)\end{aligned}$$

IV. INSPIRAL-MERGER-RINGDOWN MODEL

A. Summary of SEOBNRV5 gravitational modes

In constructing a full, semianalytical EOB model to produce waveforms for an inspiral-merger-ringdown (IMR) model, one requires three necessary components. The first is a two-body Hamiltonian which encodes the conservative EOB dynamics. It is from this Hamiltonian that one obtains the equations of motion. In this work, we completely codify this conservative sector with our PS-gauge Hamiltonian informed with SF data and then additionally supplemented with PN information that was presented in the previous section. The other two components required to complete our model are the EOB *radiation-reaction forces* and the *gravitational modes*. To complete our model, we employ the SEOBNRV5 waveform model built for the fourth LVK observing run (O4)[6] [104]. SEOBNRV5 is an IMR multipolar waveform model developed for quasicircular, spinning, nonprecessing black hole binaries and was introduced in a series of articles [50,52,53,105]. SEOBNRV5 is particularly advantageous for our use since the software package for its use, PYSEOBNR, has been built in a very modular fashion in the PYTHON language. A detailed overview of this software package can be found in Ref. [105]. The PYSEOBNR framework is suitably flexible in that the radiation-reaction (RR) forces and gravitational modes are implemented independently of the specific form of the EOB Hamiltonian. Therefore this allows the SEOBNRV5 components used in this part of the model to remain unchanged, whilst one is free to insert an entirely new Hamiltonian.

In the following section, we briefly review the relevant SEOBNRV5 components. For a more complete and detailed discussion, we refer the reader to Refs. [50,52,53]. In the SEOBNRV5 model, the complete binary coalescence process, including the inspiral, plunge, merger, and ringdown phases, is described through the gravitational polarizations in the observer's frame,

$$h(t;\iota,\varphi_0) = h_+(t;\iota,\varphi_0) - ih_\times(t;\iota,\varphi_0), \\ = \sum_{\ell=2}^{\infty}\sum_{m=-\ell}^{\ell} {}_{-2}Y_{\ell m}(\iota,\varphi_0)h_{\ell m}(t;\boldsymbol{\lambda}), \quad (42)$$

where ι is the inclination angle of the binary's orbit relative to the observer, and φ_0 is the azimuthal orientation. The functions ${}_{-2}Y_{\ell m}(\iota,\varphi_0)$ are the -2 spin-weighted spherical harmonics and $\boldsymbol{\lambda}$ signify the intrinsic parameters of the compact binary source. In reality, since the waveform scales with the total mass, M, the waveform modes $h_{\ell m}(t;\boldsymbol{\lambda})$ are simply a function of the mass ratio q and the spins: χ_1 and χ_2. The waveform model simplifies for spin aligned/antialigned binaries with $h_{\ell m} = (-1)^\ell h^*_{\ell -m}$, reducing the number of modes necessary for analysis.

Within this framework, the seven dominant modes considered are $(\ell, m) = (2,2), (2,1), (3,3), (3,2), (4,4), (4,3)$, and (5, 5). The evolution of each mode through the coalescence stages is given by,

$$h_{\ell m}(t) = \begin{cases} h^{\text{insp}-\text{plunge}}_{\ell m}(t), & t < t^{\ell m}_{\text{match}} \\ h^{\text{merger}-\text{RD}}_{\ell m}(t), & t > t^{\ell m}_{\text{match}} \end{cases}, \quad (43)$$

where the matching times $t^{\ell m}_{\text{match}}$ are critical for transitioning between phases,

$$t^{\ell m}_{\text{match}} = \begin{cases} t^{22}_{\text{peak}}, & (\ell, m) = (2,2), (3,3), (2,1), (4,4), (3,2), (4,3) \\ t^{22}_{\text{peak}} - 10M, & (\ell, m) = (5,5) \end{cases}. \quad (44)$$

Here t^{22}_{peak} is the peak of the (2, 2)-mode amplitude, and establishes a relationship with the remnant-BH ISCO,

$$t^{22}_{\text{peak}} = t_{\text{ISCO}} + \Delta t_{\text{NR}}, \quad (45)$$

where t_{ISCO} refers to the ISCO time for a Kerr black hole characterized by the remnant's final mass and spin [106]. Δt_{NR} is a calibration parameter for aligning the EOB and NR (2, 2)-mode peaks at merger. We shall return to this calibration for our model in Sec. V A. From Eq. (44), one observes a different choice of matching time is made for the (5, 5) mode. This distinct choice is discussed in detail in Refs. [50,107].

The gravitational waveforms for the inspiral and plunge are formulated as,

$$h^{\text{insp}-\text{plunge}}_{\ell m}(t) = h^{\text{F}}_{\ell m}(t) N_{\ell m}(t), \quad (46)$$

where $h^{\text{F}}_{\ell m}(t)$ aggregates the PN expanded gravitational wave modes for circular orbits in a factorized manner [88,108,109], and $N_{\ell m}(t)$ applies nonquasicircular (NQC) corrections to account for radial effects during the plunge [110–113].

The complete factorized inspiral waveform, $h^{\text{F}}_{\ell m}$, is described by the following product [112]:

[6] SEOBNRV5 can be accessed via the PYSEOBNR PYTHON package, which is hosted at https://git.ligo.org/waveforms/software/pyseobnr. For stable releases of PYSEOBNR, users can download them from the PYTHON Package Index and install using the command: PIP INSTALL PYSEOBNR.

$$h^F_{\ell m} = h^{\rm N}_{\ell m} \hat{S}_{\ell m} T_{\ell m} f_{\ell m} e^{i\delta_{\ell m}}. \quad (47)$$

The leading term, $h^{\rm N}_{\ell m}$, represents the Newtonian contribution to the waveform, providing a foundation upon which further relativistic corrections are built. It is explicitly given by,

$$h^{\rm N}_{\ell m} = \frac{\nu M}{d_L} n_{\ell m} c_{\ell+\epsilon_{\ell m}}(\mu) v_\varphi^{\ell+\epsilon_{\ell m}} Y_{\ell-\epsilon_{\ell m},-m}\left(\frac{\pi}{2},\varphi\right), \quad (48)$$

where d_L is the luminosity distance, and $Y_{\ell m}$ the spherical harmonics. The coefficients $n_{\ell m}$ and $c_k(\nu)$ are functions that modulate the amplitude based on the orbital dynamics and read

$$n_{\ell m} = \begin{cases} \frac{8\pi(im)^\ell}{(2\ell+1)!!}\sqrt{\frac{(\ell+1)(\ell+2)}{\ell(\ell-1)}}, & \ell+m \text{ is even}, \\ \frac{-16i\pi(im)^\ell}{(2\ell+1)!!}\sqrt{\frac{(2\ell+1)(\ell+2)(\ell^2-m^2)}{(2\ell-1)(\ell+1)\ell(\ell-1)}}, & \ell+m \text{ is odd}, \end{cases} \quad (49)$$

with

$$c_k(\nu) = \left(\frac{1-\sqrt{1-4\nu}}{2}\right)^{k-1} + (-1)^k \left(\frac{1+\sqrt{1-4\nu}}{2}\right)^{k-1}. \quad (50)$$

The parity $\epsilon_{\ell m}$ of the mode is defined as

$$\epsilon_{\ell m} = \begin{cases} 0, & \ell+m \text{is even}, \\ 1, & \ell+m \text{ is odd}. \end{cases} \quad (51)$$

Furthermore, the velocity v_φ is derived from the orbital dynamics as specified by $H_{\rm EOB}$, with Ω and r_Ω denoting the angular and radial frequencies, respectively,

$$\Omega = \frac{\partial H_{\rm EOB}}{\partial p_\varphi}, \qquad v_\varphi = M\Omega r_\Omega, \qquad \frac{1}{r_\Omega^{3/2}} = \left.\frac{\partial H_{\rm EOB}}{\partial p_\varphi}\right|_{p_r=0}. \quad (52)$$

The term $\hat{S}_{\ell m}$ acts as an effective source term for the waveform, with its form determined by the parity of the mode

$$\hat{S}_{\ell m} = \begin{cases} \hat{H}_{\rm eff}, & \ell+m \text{ is even}, \\ \sqrt{x}\hat{p}_\varphi & \ell+m \text{ is odd}, \end{cases} \quad (53)$$

where $v_\Omega = (M\Omega)^{1/3}$, and $\hat{H}$eff and $\hat{p}_\varphi$ denote the reduced effective energy and the orbital angular momentum, respectively, each normalized by its Newtonian counterpart.

The component $T_{\ell m}$ incorporates the leading-order tail effects through a resummation of an infinite number of leading logarithms [114], such that

$$T_{\ell m} = \frac{\Gamma(\ell+1-2i\hat{\Omega})}{\Gamma(\ell+1)} e^{\pi m\hat{\Omega}} \left(\frac{4mM\Omega}{\sqrt{e}}\right)^{2im\hat{\Omega}}, \quad (54)$$

where $\hat{\Omega} = \Omega H_{\rm EOB}$ represents the normalized orbital frequency by the total energy, and $\Gamma(.)$ is the Euler gamma function.

Finally, the amplitude and phase $f_{\ell m}$ and $\delta_{\ell m}$ are polynomials in the velocity, whose coefficients are determined by requiring that the factorized modes agree with the expanded PN expressions. For brevity, we do not reproduce the full expressions here and instead refer the reader to Appendix B of Ref. [50], where they are given in full for SEOBNRV5. In the nonspinning case, the amplitude is further resummed according to $f_{\ell m} = (\rho_{\ell m})^\ell$, in order to mitigate the linear-in-ℓ growth of the 1PN coefficient in $\rho_{\ell m}$. The function $f_{\ell m}$ is then given by,

$$f_{\ell m} = \begin{cases} (\rho_{\ell m})^\ell, & m \text{ is even}, \\ (\rho_{\ell m})^\ell + f^{\rm S}_{\ell m}, & m \text{ is odd}, \end{cases} \quad (55)$$

where $f^{\rm S}_{\ell m}$ denotes the spin-dependent contribution to the amplitude. Similar resummations can be also be found in other EOB models, for example in TEOBRESUMS in Refs. [55–57,115,116].

As described in Ref. [52], SEOBNRV5 includes additional calibration of both the waveform modes and the RR force in the nonspinning sector using 2GSF flux data [79]. One considers the expansion of the $\rho_{\ell m}$ in the terms of the symmetric mass ratio,

$$\rho_{\ell m} = \rho^{(0)}_{\ell m} + \nu\rho^{(1)}_{\ell m} + \mathcal{O}(\nu^2). \quad (56)$$

The linear in mass-ratio term, $\rho^{(1)}_{\ell m}$, is then modified by a correction term, $\Delta\rho^{(1)}_{\ell m}$, determined by fitting to SF results for the linear in mass-ratio term. After the publication of the SEOBNRV5 model [50,52], the authors of Ref. [79] discovered an error in their data, which was used for the calibration. While redoing the calibration with the corrected SF data, an inconsistency was found with the way the SF-calibration was propagated to the waveform modes in Ref. [52]. When consistently computing the flux and waveform, the 2GSF calibration should yield distinct correction terms for the RR force *and* the waveform modes. These findings will be addressed in detail in a forthcoming erratum.

In this work, we incorporate the corrected $\Delta\rho^{(1)}_{\ell m}$ flux terms, but not those for the waveform modes. This is justified because the amplitude corrections enter nominally at second post-adiabatic order, where additional effects (e.g., waveform phase corrections) that are not currently included in SEOBNRV5 also become relevant. Nevertheless, we find that when including the waveform-mode SF corrections, the

performance of the model is not significantly improved and the results for the unfaithfulness only marginally change for comparable-mass systems.

The correction terms $\Delta\rho^{(1)}_{\ell m}$ used in this work are given below, with differences from the original coefficients in Ref. [52] highlighted in bold:

$$\Delta\rho^{(1)}_{22} = \mathbf{20.6}v^8_\Omega - \mathbf{410}v^{10}_\Omega, \tag{57a}$$

$$\Delta\rho^{(1)}_{21} = 1.65v^6_\Omega + \mathbf{24.3}v^8_\Omega + 80v^{10}_\Omega, \tag{57b}$$

$$\Delta\rho^{(1)}_{33} = 12v^8_\Omega - \mathbf{222}v^{10}_\Omega, \tag{57c}$$

$$\Delta\rho^{(1)}_{32} = \mathbf{-0.25}v^6_\Omega - 6.5v^8_\Omega + 98v^{10}_\Omega, \tag{57d}$$

$$\Delta\rho^{(1)}_{44} = -3.56v^6_\Omega + \mathbf{15.3}v^8_\Omega - 216v^{10}_\Omega, \tag{57e}$$

$$\Delta\rho^{(1)}_{43} = -0.654v^4_\Omega - \mathbf{3.73}v^6_\Omega + \mathbf{18}v^{10}_\Omega, \tag{57f}$$

$$\Delta\rho^{(1)}_{55} = \mathbf{-2.608}v^4_\Omega + \mathbf{1.13}v^6_\Omega - \mathbf{35.1}v^{10}_\Omega. \tag{57g}$$

The nonquasicircular corrections, $N_{\ell m}(t)$, for SEOBNRV5 have the following form:

$$N_{\ell m} = \left[1 + \frac{p^2_{r_\star}}{(r\Omega)^2}\left(a_1^{h_{\ell m}} + \frac{a_2^{h_{\ell m}}}{r} + \frac{a_3^{h_{\ell m}}}{r^{3/2}}\right)\right] \times \exp\left[i\left(b_1^{h_{\ell m}}\frac{p_{r_\star}}{r\Omega} + b_2^{h_{\ell m}}\frac{p^3_{r_\star}}{r\Omega}\right)\right], \tag{58}$$

with the constants $a_i^{h_{\ell m}}$ and $b_i^{h_{\ell m}}$ ($i \in [0,3]$) fixed such that the EOB modes match the equivalent modes from NR at the point $t_{\rm match}$. It is important to state here, that unlike the TEOBRESUMS models and earlier iterations of SEOBNR, the NQCs in SEOBNRV5 do not enter the RR forces for the model [50,52].

The merger-ringdown EOB gravitational waveform modes, $h^{\rm merger-RD}_{\ell m}(t)$, are independent of the inspiral-plunge modes but they are smoothly connected to the inspiral-merger waveform by requiring continuity and differentiability of the waveform at merger. The merger-ringdown modes are based upon a phenomenological ansatz given explicitly in [50,107,117,118], which is then supplemented by NR simulations as well as TML waveforms [119,120]. Once again, we direct the reader to Ref. [50], for a detailed overview of their construction. It suffices to state that the merger-ringdown modes incorporated in the model presented herein are identical to those utilized in SEOBNRV5.

B. SEOBNRV5 equations of motion and radiation-reaction force

The EOB equations of motion are given by

$$\frac{dr}{dt} = \xi\frac{\partial H}{\partial p_{r_\star}}, \qquad \frac{dp_{r_\star}}{dt} = -\xi\frac{\partial H}{\partial r} + \frac{p_{r_\star}}{p_\varphi}\mathcal{F}_\varphi,$$
$$\frac{d\varphi}{dt} = \frac{\partial H}{\partial p_\varphi}, \qquad \frac{dp_\varphi}{dt} = \mathcal{F}_\varphi. \tag{59}$$

Here we use the tortoise-coordinate radial momentum $p_{r_\star}$ as opposed to the canonical radial momentum, p_r. This choice enhances the stability of the equations of motion throughout the plunge phase and near the merger, as documented in Refs. [110,121]. In the usual Hamiltonian prescription in Eq. (4) for nonspinning binaries, the tortoise-coordinate r_* is defined as in [112] by

$$\frac{dr_*}{dr} = \frac{1}{\xi(r)}, \qquad \xi(r) \coloneqq A(r)\sqrt{\bar{D}(r)}, \tag{60}$$

with the conjugate momentum p_{r_*} given by

$$p_{r_*} = p_r\xi(r). \tag{61}$$

These definitions simplify in the PS gauge, since $A(r)$ and $\bar{D}(r)$ are taken to be in the Schwarzschild TML, hence

$$\xi_{\rm PS}(r) = f(r) = 1 - \frac{2M}{r}. \tag{62}$$

The RR force in this setup, $\mathcal{F}_\varphi$, is found from the summation of the EOB gravitational waveform modes,

$$\mathcal{F}_\varphi = -\frac{\mathcal{F}^{\rm EOB}}{M\Omega} = -\frac{1}{M\Omega}\sum_{\ell=2}^{8}\sum_{m=1}^{\ell}\mathcal{F}^{\rm EOB}_{\ell m}, \tag{63}$$

where the (ℓ, m)-contributions are found directly from the inspiral-plunge waveform modes in Eq. (46) such that

$$\mathcal{F}^{\rm EOB}_{\ell m} = d_L^2\frac{(mM\Omega)^2}{8\pi}|h^{\rm F}_{\ell m}|^2. \tag{64}$$

V. CALIBRATION TO NUMERICAL-RELATIVITY WAVEFORMS

We shall now explore the calibration pipeline for our model with NR simulations. For the full SEOBNRV5 model, there are three calibration parameters: $(a_6, d_{\rm SO}, \Delta t_{\rm NR})$, which are each a function of the binary parameters $\boldsymbol{\lambda}$, and are designed to improve the agreement with binary BH simulations. The a_6 parameter replaces the partially known 5PN-coefficient (u^6-coefficient) in the DJS-gauge $A(u)$ potential, whilst the second parameter,

$d_{\rm SO}$, is a 4.5PN spin-orbit parameter [50]. Since our model is in the nonspinning regime and our primary potential is informed through SF information rather than purely a PN expansion, we do not explore calibration parameters akin to a_6 and $d_{\rm SO}$ in this work. In this section our focus will therefore be on the sole calibration parameter $\Delta t_{\rm NR}$.

Introduced in Eq. (45), $\Delta t_{\rm NR}$ is a parameter that determines the time shift between the ISCO, computed from the final mass and spin of the remnant object [122,123] and the peak of the (2, 2)-mode amplitude. The idea is to allow $\Delta t_{\rm NR}$ to be a freely varying parameter that is determined by minimizing the discrepency of the waveforms' peak time, between EOB and NR, at the end of the inspiral-plunge stage (i.e. $t < t_{\rm match}$). To do this we calibrate our model in a similar manner to SEOBNRV5 as outlined in Ref. [50], to a set of nonspinning NR waveforms all generated using the pseudo-Spectral Einstein code from the Simulating eXtreme Spacetimes (SXS) collaboration [27,28,30,31,118,124–131]. This publicaly available subset of nonspinning waveforms spans mass ratios in the range $1 < q < 20$ and forms part of the larger set used for the full calibration procedure described in Ref. [50], which covers a broader region of parameter space. They are the same set of NR simulations used in SEOBNRV5 and SEOBNRV5-PM. The specific simulations used in this work are listed in Table I of Appendix C.

A crucial aspect required to be able to calibrate an EOB waveform to an NR waveform is an appropriate measure to establish the difference between two waveforms. Therefore we define the noise-weighted inner product, $(h_1|h_2)$, between two different waveforms, $h_1(t)$ and $h_2(t)$ [132,133],

$$(h_1|h_2) \coloneqq 4\mathrm{Re}\left[\int_{f_l}^{f_h} \frac{\tilde{h}_1(f)\tilde{h}_2^*(f)}{S_n(f)}\mathrm{d}f\right]. \tag{65}$$

Here, $S_n(f)$ is the one-sided power spectral density of the detector noise of advanced LIGO, see Ref. [134], and $\tilde{h}_i$ denotes the Fourier transform of the waveform h_i. We also fix $f_h = 2048$ Hz. The second limit of integration, f_l, is dependent on the type of waveforms that enter the inner product. If the two waveforms are in band, such as when one is comparing two different EOB waveform models, $f_l = 10$ Hz. However, when one is comparing to NR waveforms, we set f_h to have a buffer factor such that $f_l = 1.35 f_{\rm start}$, where $f_{\rm start}$ is the peak of the NR waveform in the frequency domain. The inclusion of the buffer factor is to ensure that any spurious features that enter into the inner product due to the Fourier transform of the time-domain NR waveform are excluded from the calculation of the inner product. This inner product is then used to calculate the *faithfulness*, between two waveforms

$$\langle h_1|h_2\rangle = \max_{\delta\phi,\delta t} \frac{(h_1(\delta\phi,\delta t)|h_2)}{\sqrt{(h_1|h_2)(h_1|h_2)}}, \tag{66}$$

which is the overlap over the two waveforms maximized over the time and phase shift, δt and $\delta\phi$, respectively. One can then use the faithfulness to define the *unfaithfulness*, otherwise known as *mismatch*, between an EOB waveform an NR waveform, denoted $h_{\rm EOB}$ and $h_{\rm NR}$, respectively,

$$\mathcal{M}(\boldsymbol{\theta}) \coloneqq 1 - \langle h_{\rm EOB}(\boldsymbol{\lambda};\boldsymbol{\theta})|h_{\rm NR}(\boldsymbol{\lambda})\rangle. \tag{67}$$

Here, we have introduced $\boldsymbol{\theta}$ as the generic set of calibration parameters. Unlike in Ref. [50], in this work we are only exploring the use of a single calibration parameter such that $\boldsymbol{\theta} \coloneqq \Delta t_{\rm NR}$.

A. Calibration of $\Delta t_{\rm NR}$

In calibrating our $\Delta t_{\rm NR}$[7] parameter, we adopt the same strategy as Ref. [50] that was used in the calibration of the SEOBNRV5 model, which itself was based on the methods used in calibrating the previous version in this family of EOB models, SEOBNRV4 [135,136]. Our aim is to fix the calibration parameter by creating a fit over the binary parameter space. Since we are only considering nonspinning, quasicircular binary systems, the fit shall only be dependent on the symmetric mass ratio and is obtained by sampling over each nonspinning quasicircular NR simulation. One samples over a one-dimensional grid to obtain a posterior distribution the $\Delta t_{\rm NR}$ parameter for each NR simulation from a uniform prior, before taking a direct fit of the maximum-likelihood point of the posterior distributions. Note that, unlike the calibration procedure described in Ref. [50], the calibration procedure here does not require the use of a Markov-chain Monte Carlo method and, consequently, does not require a nested sampling algorithm, as our calibration parameter space is one-dimensional rather than multidimensional. This would change if one was considering a more complete calibration procedure with extra PN and spinning calibration parameters as is the case with SEOBNRV5.

We define the maximum likelihood as

$$P(h_{\rm NR}|\boldsymbol{\theta}) \propto \exp\left[-\frac{1}{2}\left(\frac{\mathcal{M}_{\rm max}(\boldsymbol{\theta})}{\sigma_{\mathcal{M}}}\right)^2 - \frac{1}{2}\left(\frac{\delta t_{\rm merger}(\boldsymbol{\theta})}{\sigma_t}\right)^2\right], \tag{68}$$

where $\mathcal{M}_{\rm max}$ is the maximum unfaithfulness over total mass between the NR and EOB waveforms, see Eq. (67), and $\delta t_{\rm merger}$ is the difference in the merger[8] times of the NR and EOB waveforms. We choose the parameters, $\sigma_{\mathcal{M}}$ and σ_t, to be 10^{-3} and $5M$, respectively, which are the same values used in the calibration of SEOBNRV5 [50]. This

[7]Note in Ref. [50], what we refer to as $\Delta t_{\rm NR}$ was labeled as $\Delta t^{22}_{\rm ISCO}$.

[8]In this context the merger time is defined as the peak of the amplitude of the (2, 2) mode.

maximum likelihood is the measure on which we perform the basis of our fitting procedure.

During the sampling routine, we assume uniform priors for the calibration parameter and vary over the range $\Delta t_{\rm NR} \in [-100, 40]$ to obtain posterior distributions for $P(h_{\rm NR}|\boldsymbol{\theta})$. One difficulty that arises for some values of posterior distributions is multimodality. That is, secondary modes can appear for certain values of the binary parameters, $\boldsymbol{\theta}(\boldsymbol{\lambda})$. These modes would spoil a potential fitting of the calibration parameter and so to ensure a more uniform fit, we choose just one mode from each calibration posterior, considering continuity. In practice, one can directly discard samples from the original posterior, but here we choose to separate the distributions through fitting the posterior using a *Gaussian mixture model* through the SKLEARN.MIXTURE package [137]. This model assumes the distribution is made of a mixture of Gaussian distributions, each with its own mean and covariance. Therefore it is particularly effective for capturing the presence of subpopulations within an overall population, without requiring prior knowledge of which subpopulation an observation belongs to. The model parameters are estimated using the expectation-maximization algorithm [137], which iteratively assigns a "soft" membership of each data point to a particular Gaussian component and updates the Gaussian parameters accordingly. The process continues until convergence, yielding a robust separation of the posterior into distinct modes. Once this analysis is complete, we identify bimodal posteriors and retain only the component corresponding to the dominant mode, extracting its mean, variance, and maximum-likelihood estimate.

An example multimodal posterior is given in Fig. 2. We find a correlation between the appearance of multimodal posteriors and more comparable mass-ratio simulations. These correlations manifest themselves for mass-ratios $\nu \gtrsim 0.14$ ($q \lesssim 5$), the region of the parameter space where we expect the small-mass ratio approximation of the SF expansion to be at its least accurate.

After processing the posteriors when appropriate, we also leverage information of the conservative dynamics in the TML to extrapolate our fit to the $\nu \to 0$ limit using Ref. [120] in the same way as done in Ref. [50]. The resultant posteriors and TML value are then fitted directly using a least-squares-fitting procedure and a rational function. In our investigations, we find that a different choice of rational function works better for each variant of the model with 3PN and 4PN corrections. For the model with 3PN corrections, the same rational function as Ref. [50] produces a more natural fit, given by

$$\Delta t^{\rm 3PN}_{\rm NR} = (a^3_0 + a^3_1\nu + a^3_2\nu^2 + a^3_3\nu^3)\nu^{-1/5+a^3_4\nu}, \quad (69)$$

where $a_i (i \in [0, 4])$ are constants determined by the fitting procedure. Note with this we retain the same functional form as Ref. [50] including the expected test mass scaling

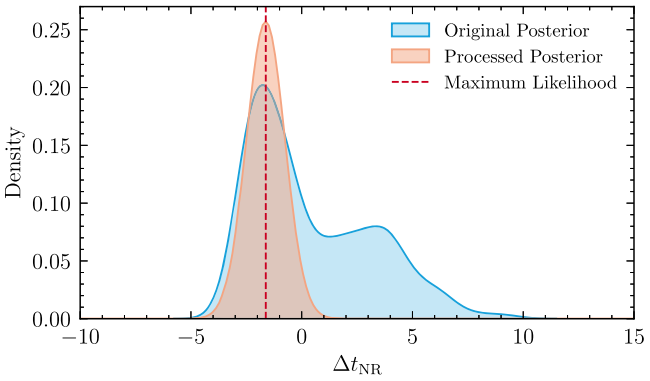


FIG. 2. An example of a multimodal posterior for the calibration parameter $\Delta t_{\rm NR}$ for SXS:BBH:2425 ($q = 2.0, \chi_1 = \chi_2 = 0.0$). The blue posterior is the initial result we obtain from our sampling over the range of $\Delta t_{\rm NR}$ values and exhibits two distinct regions or *modes* which the values cluster around. The second, orange, posterior is a processed posterior where we have removed the mode corresponding to the positive value of $\Delta t_{\rm NR}$ as this would lead to irregular fit of the calibration parameter.

of $t_{\rm peak} - t_{\rm ISCO}$ with the $\nu^{-1/5}$ factor [45]. For the model with the 4PN corrections, however, we find a more reasonable fit using a fitting function inspired by a *post-leading-transition expansion* in Ref. [138],

$$\Delta t^{\rm 4PN}_{\rm NR} = (a^4_0 + a^4_1\nu^{1/5} + a^4_2\nu^{2/5} + a^4_3\nu^{3/5} + a^4_4\nu^{4/5})\nu^{-1/5}, \quad (70)$$

which better fits the resulting trend of the posteriors. The resultant fits for the 3PN and 4PN corrected versions of the SEOBNR-GSF models are shown in Fig. 3, which we refer to as $\Delta t^{\rm 3PN}_{\rm NR}$ and $\Delta t^{\rm 4PN}_{\rm NR}$, respectively. Explicitly, the fitting coefficients for the calibration parameter for both models read,

$$\begin{aligned}
a^3_0 &= 6.06749591,\\
a^3_1 &= -58.53430766,\\
a^3_2 &= -274.89832051,\\
a^3_3 &= 2552.05275465,\\
a^3_4 &= -1981.68604241,\\
a^4_0 &= -205.15155028,\\
a^4_1 &= 1188.35994636,\\
a^4_2 &= -3307.97319917,\\
a^4_3 &= 4191.43478856,\\
a^4_4 &= -1876.6265344. \quad (71)
\end{aligned}$$

As mentioned previously, we do not seek a calibration parameter akin to the a_6 parameter employed in the SEOBNRV5 model since our model is primarily informed

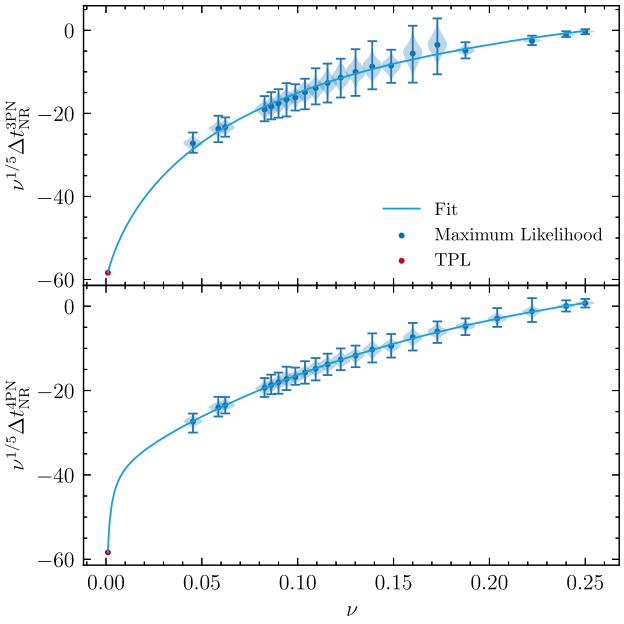


FIG. 3. Fits for the $\Delta t_{\rm NR}$ calibration parameter for the 3PN and 4PN SEOBNR-GSF models. One obtains the calibration parameter as a function of the mass-ratio ν from a least squares fit of the maximum likelihood of the posteriors (blue shaded violins) for a set of nonspinning NR simulations and TML values. As done for SEOBNRV5 in Ref. [50], we adopt the rescaling by $\nu^{1/5}$, which substantially improves the agreement in the test-particle limit where $\nu \to 0$.

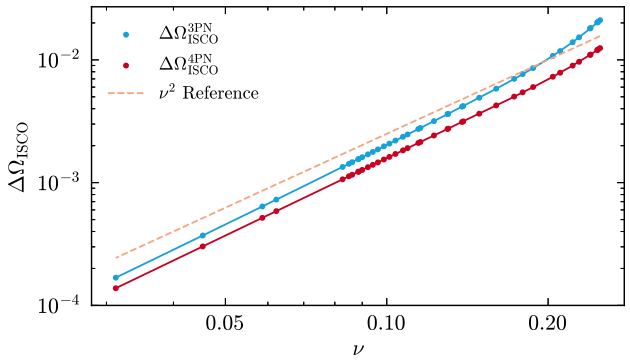


FIG. 4. Residuals of the ISCO frequency shift relative to the first-order GSF expansion. As expected, both the 3PN and 4PN versions of the SEOBNR-GSF model exhibit the correct TML behavior: the residuals scale as ν^2, consistent with the next-to-leading order in the GSF expansion as $\nu \to 0$. The curves show residuals computed from ISCO frequency shift values extracted from the publicly available nonspinning NR simulations in the SXS catalogue.

from GSF information. But, the a_6 calibration parameter in the TML is tuned using data for the frequency shift of the ISCO calculated using GSF results [83,90,139] such that

$$M\Omega_{\rm ISCO}^{\rm 1SF} = 6^{-3/2}(1 + C_\Omega/q),$$
$$C_\Omega = 1.25101539 \pm 4 \times 10^{-8}. \tag{72}$$

Therefore, one would expect a GSF-informed model would capture this ISCO frequency shift in the TML. In the EOB formalism, the ISCO can be computed directly from the EOB Hamiltonian by finding the point in phase space (r, p_φ) where the first and second derivatives of the Hamiltonian vanish when $p_r = 0$,

$$\left.\frac{\partial^2 H}{\partial r^2}\right|_{p_r=0} = \left.\frac{\partial H}{\partial r}\right|_{p_r=0} = 0. \tag{73}$$

We find that both of our SF models produce agreement with the $\Omega_{\rm ISCO}^{\rm 1SF}$ value in the TML with a relative error of $\lesssim 0.4\%$, whilst SEOBNRV5, without calibration of the a_6 parameter to account for the ISCO shift, yields a value with a relative error of $\sim 6.7\%$. Furthermore, one can assess the scaling of the residual of the frequency shift calculated from the EOB model and the GSF expansion of Eq. (72). As one can see in Fig. 4, we obtain the expected ν^2 scaling in the limit $\nu \to 0$ for the residual of the frequency shift, denoted $\Delta\Omega_{\rm ISCO}$, for both flavors of the SEOBNR-GSF model. It should also be noted, although we have not included the result in the plot for visual simplicity, that the SEOBNRV5 model without the a_6 calibration does not reproduce the same behavior in the TML.

VI. RESULTS

A. Binding energy

The first assessment of the performance of our model is to compare the binding energy of the binary system. This serves as a complimentary assessment to the computing of the unfaithfulness with NR waveforms, giving us an insight into how the information from the two-body dynamics is encoded in the resummation of the conservative dynamics that forms our model. A similar comparison was completed in Ref. [84]. In Fig. 5 we present the fractional difference between the EOB binding energy, $E_{\rm bind}^{\rm EOB}$, and the binding energy obtained from NR simulations for four different mass ratios, using the 3PN and 4PN models, respectively, as well as the SEOBNRV5 model calibrated solely with the $\Delta t_{\rm NR}$ parameter. For the NR simulations, we utilize the binding energy obtained in Ref. [140]. The binding energies in both panels of Fig. 5 are plotted as a function of the quasicircular velocity parameter, v_Ω, where the orbital frequency $\Omega = \Omega_{\rm NR}$ for the NR simulations and $\Omega_{\rm EOB}$ is the orbital frequency for the EOB models. In particular, $\Omega_{\rm EOB}$ is obtained directly from $\Omega_{\rm EOB} = \partial H/\partial\varphi$ to ensure there is no gauge ambiguity between the EOB models and the definition used in NR simulations [140]. It should be emphasized that the EOB binding energy here is evaluated along the orbital dynamics.

We see very good agreement between our new EOB models and NR up to a few cycles before merger, with markedly better agreement for our 4PN model, which remains

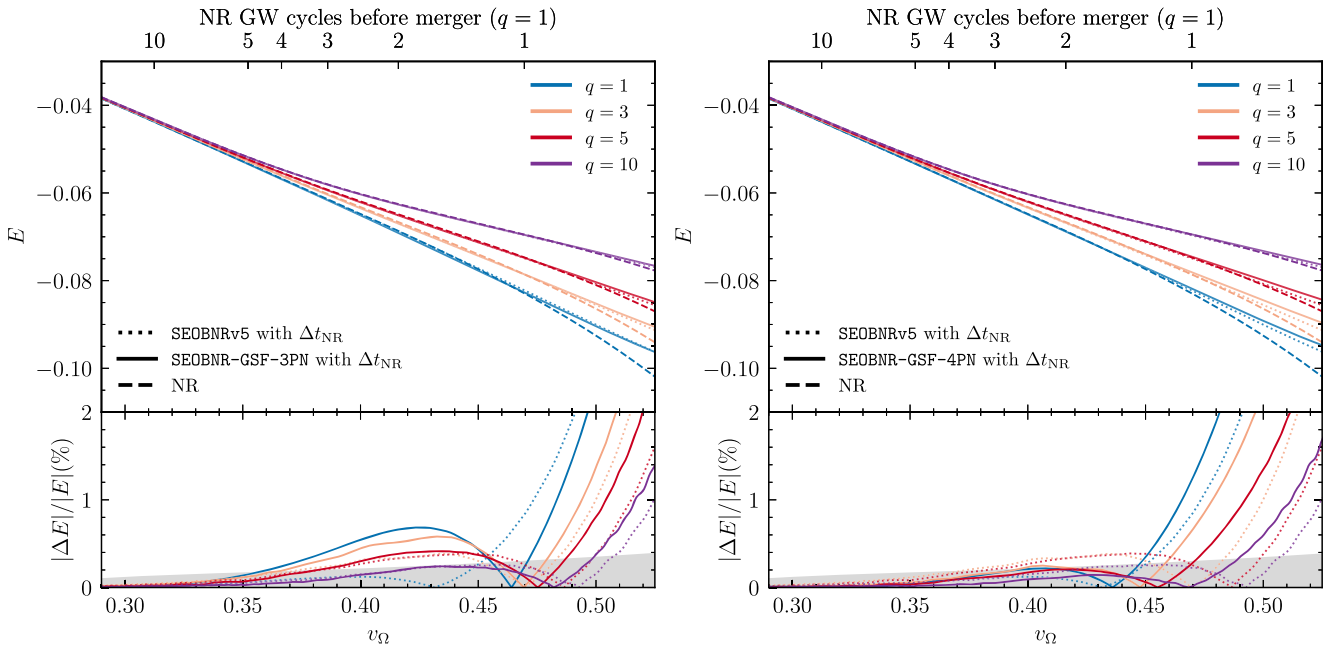


FIG. 5. Nonspinning binding energy as a function of the orbital velocity, $v_\Omega = (M\Omega)^{1/3}$, is presented for the SEOBNRV5 model with a calibrated $\Delta t_{\rm NR}$ parameter and the SEOBNR-GSF model incorporating 3PN corrections (left plot) and 4PN corrections (right plot), both with a calibrated $\Delta t_{\rm NR}$ parameter for a range of mass-ratios $q \in [1, 10]$. The upper panels show the binding energy ($E = E_{\rm bind}$) as a function of v_Ω along the orbit, whilst the lower panels show the fractional difference (where $\Delta E = E^X_{\rm bind} - E^{\rm NR}_{\rm bind}$) between the EOB binding energies for the various models and the NR simulations across different mass-ratios. The shaded region indicates an estimate of the uncertainty of the NR simulation for $q = 1$, as provided in Ref. [140], and similarly for 4PN, and SEOBNRV5 with $\Delta t_{\rm NR}$.

within the uncertainty of our NR simulations up to one cycle before merger. This is a similar level of accuracy that we see with SEOBNRV5, as is evident from both figures. Unsurprisingly, this shows that the SEOBNR-GSF models with 4PN corrections perform better than the model with only up to 3PN corrections. Therefore in our waveform performance comparisons in the next section, we only consider comparisons with the SEOBNR-GSF model with 4PN corrections to avoid unnecessary comparisons. Henceforth, any plot of SEOBNR-GSF will be referring to the model with 4PN corrections unless explicitly stated otherwise.

B. Comparison to 1PAT1 waveforms

The crucial measure of our model's performance lies in the quality of the waveforms it generates. In Figs. 6 and 7, we present a comparison of the (2, 2) mode of the SEOBNR-GSF waveforms with those generated directly from 2GSF calculations, specifically the 1PAT1 variant [81], as well as with NR waveforms from the SXS catalogue. This comparison is conducted for both low mass ratios ($q = 1, 4$) in Fig. 6 and high mass ratios ($q = 10$, 15) in Fig. 7.

A detailed overview of the 1PAT1 GSF waveform model, and the approximations made therein, is found within Sec. II of Ref. [142]. We briefly outline the important details here for our subsequent discussion.

The 1PAT1 model is based on a *multiscale expansion* of Einstein's field equations, where the metric perturbation is expanded to separate the slow evolution of the binary's orbital frequency, Ω, from the rapidly evolving phase, φ. In this framework, the slow evolution occurs on the radiation-reaction timescale, $t_{\rm RR} \sim (q\Omega)^{-1}$, while the orbital phase evolves on the much shorter orbital timescale, $t_{\rm orb} \sim (\Omega)^{-1}$. These timescales are treated independently in the analysis.

This decomposition results in a set of Fourier-domain partial differential equations (PDEs) for the amplitudes of the metric perturbation at a fixed Ω and a separate set of ordinary differential equations governing the evolution of the binary's mechanical parameters, Ω and φ. The Fourier-domain PDEs are further simplified through a multipole decomposition, and by imposing the Lorenz-gauge condition [143]. Solving these field equations as an offline step has been the main challenge in second-order SF calculations. This has prompted a series of works exploring the groundbreaking calculations required for this step [144–149].

The discussion in Ref. [142] also highlights the domain of validity for the 1PAT1 model, which are valid only during the inspiral and break down toward the ISCO. The reason for this breakdown lies within the assumptions of the multiscale expansion. Implicitly, the expansion we have described assumes the secondary BH in the binary configuration follows a quasicircular inspiral, whereby the variation of the orbital frequency is such that $\dot{\Omega} \sim \mathcal{O}(q)$. But this assumption breaks down close to the ISCO in such a way for one encounters unphysical divergences in the

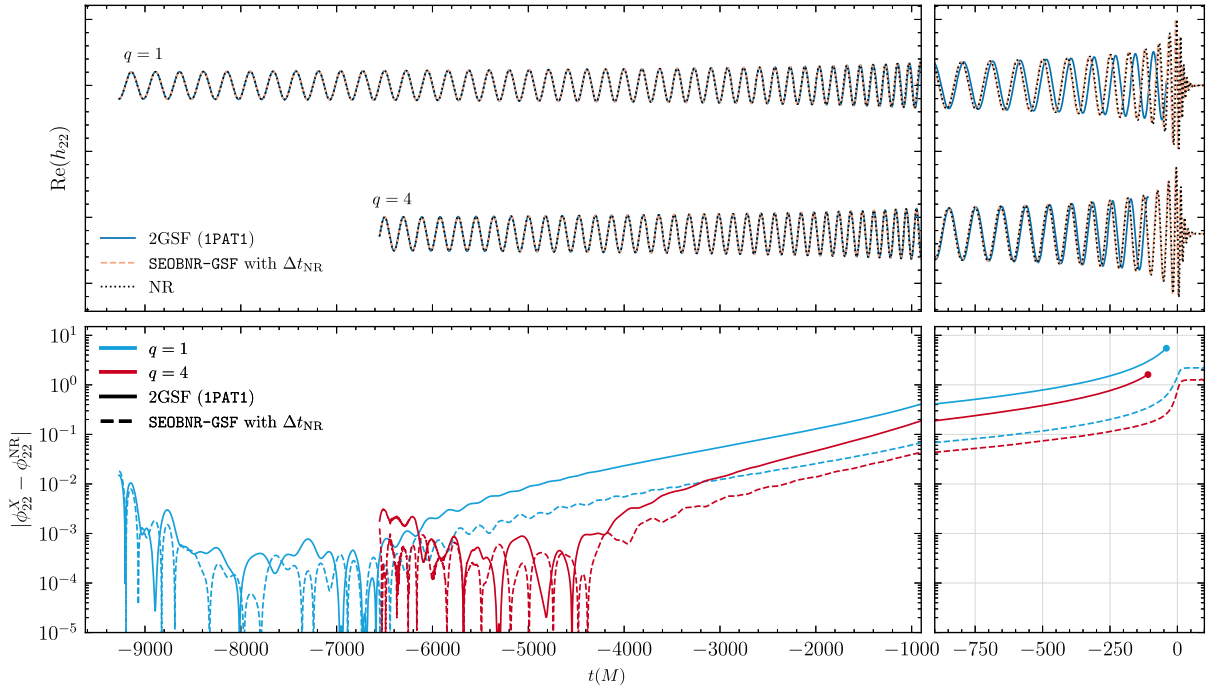


FIG. 6. Top panel: A comparison of the (2, 2) waveform modes of the 1PAT1 model, the SEOBNR-GSF model and NR simulations at mass ratios $q = 1$ and $q = 4$. The waveforms are aligned at early times using the procedure originally outlined in Ref. [141]. Bottom panel: The phase difference between the two models and the NR simulations for the waveforms plotted in the top panel. In both panels, we magnify last $-900M$ before merger [peak of the (2, 2)-mode amplitude] and end the 1PAT1 waveforms at v_Ω. One observes at these small mass-ratios, the SEOBNR-GSF model has a markedly smaller phase difference when compared to the 1PAT1 model, particularly toward the late inspiral toward $v_\Omega^{\rm break}$, where the multiscale expansion breaks down. Furthermore, the SEOBNR-GSF model includes all stages of the binary coalescence through inspiral, merger and ringdown.

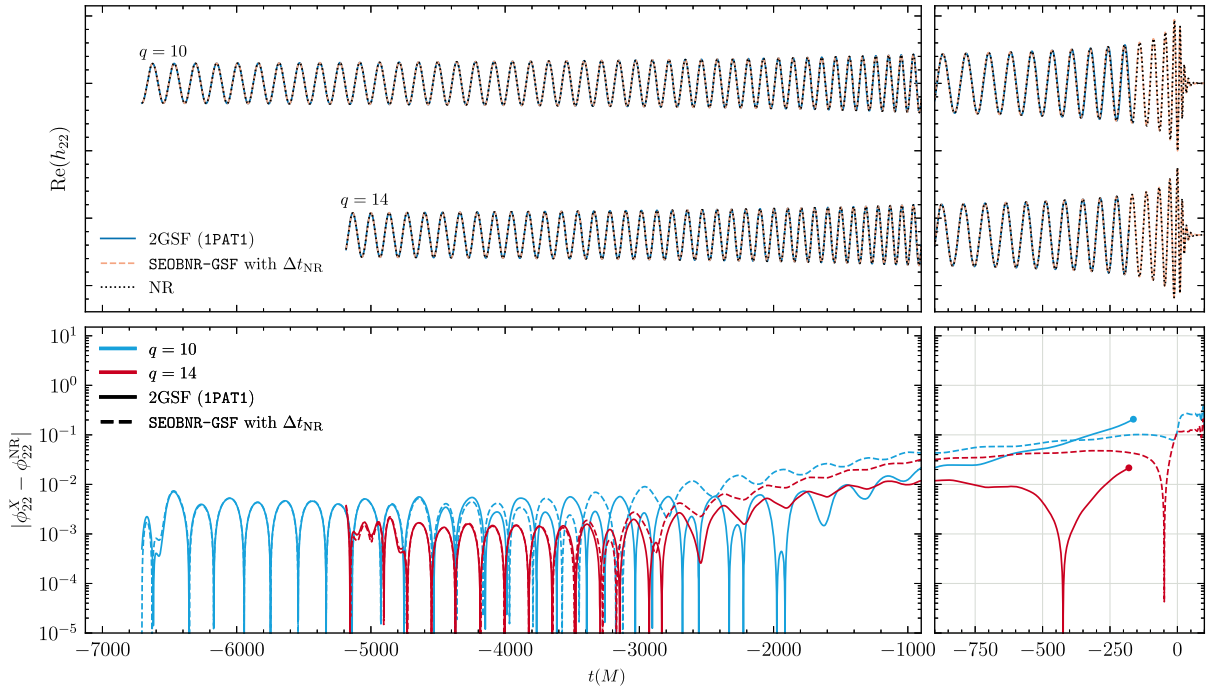


FIG. 7. Top panel: A comparison of the (2, 2) waveform modes of the 1PAT1 model, the SEOBNR-GSF model and NR simulations at mass-ratios $q = 10$ and $q = 15$. Bottom panel: The phase difference between the two models and the NR simulations for the waveforms plotted in the top panel. For these higher mass-ratios, the SEOBNR-GSF model has a comparable phase difference when compared to the 1PAT1 model, with the main difference being the SEOBNR-GSF model does not break down before the merger.

multiscale expansion of the field equations, leading to inaccuracies in the solutions to the field equations and quantities calculated therefrom, including the second-order fluxes and therefore the waveforms from the 1PAT1 model. To quantify where this limit of the model occurs, Ref. [142] (and subsequently reported in Ref. [52]) provided an estimate for where multiscale expansion breaks down,

$$v_\Omega^{\rm break} = v_\Omega^{\rm ISCO} - 0.052\nu^{1/4}, \tag{74}$$

$$v_\Omega^{\rm ISCO} = \frac{1}{\sqrt{6}} \simeq 0.408. \tag{75}$$

We indicate this breakdown in both Figs. 6 and 7 with dots at the end of the phase difference in the bottom panels.

Immediately, in the top panel of each figure, one can distinguish the main difference between SEOBNR-GSF and 1PAT1 is that our EOB model includes the complete binary coalescence through inspiral, merger and ringdown whilst the 2GSF model breaks down toward merger as expected. Remarkably, however, in the early inspiral regime, the waveforms are indiscernible from each other, it is only through looking at the phase difference in the bottom panels that we are able to separate them. The dephasing between the two models and NR simulations at lower mass ratios is more pronounced in later stages of the inspiral, yet the phase difference between the 1PAT1 waveforms and NR still remains $\lesssim$0.3 radians even $\sim 900M$ before merger. In the same regime, the SEOBNR-GSF waveforms perform better for the same mass ratios where the dephasing between the waveforms and NR are still below $\sim$0.1 radians. It is important that a similar study was conducted for similar mass-ratios for SEOBNRV5 in Ref. [52], which showed a comparable level of dephasing.

For the more intermediate mass-ratio comparison in Fig. 7, we see the 1PAT1 model remain at a more comparable level of dephasing to SEOBNR-GSF. For $q = 10$ and $q = 15$, one sees that the 1PAT1 model only dephases by $\sim$0.5 radians by the estimated break down at $v_\Omega \sim 150M$ before merger, with SEOBNR-GSF at a similar level of dephasing. The clear advantage of SEOBNR-GSF for these intermediate mass ratios is that the model maintains this level of dephasing while continuing through the latter stages of the inspiral, up to and including the merger and postmerger regime.

C. Inspiral-merger-ringdown comparison

Since SEOBNR-GSF generates complete IMR waveforms, rather than only covering the inspiral phase, one can perform a more comprehensive assessment of the model's performance by calculating the mismatch with NR waveforms. We introduced the mismatch in Eq. (67) for calculating our calibration parameter, but now we shall use this as a test of the performance of SEOBNR-GSF. We calculate the mismatch of SEOBNR-GSF for a set of SXS NR nonspinning waveforms, which were also used in the calibration and assessment of SEOBNRV5 in Refs. [50,52]. The mismatches are calculated over a range of the binary's total mass range $10M_\odot \leq M \leq 300M_\odot$ for the $(\ell, m) = (2, 2)$ mode.

To assess the impact of adding the conservative 1GSF corrections to the Hamiltonian we compare to two other variants of the SEOBNR waveform family. We consider a version of SEOBNRV5 without any calibration of the Hamiltonian, only calibrating the $\Delta t_{\rm NR}$ parameter, which we will refer to as "SEOBNRV5 with $\Delta t_{\rm NR}$." However, SEOBNRV5 differs from SEOBNR-GSF not only in the physical content included in the Hamiltonian, but also in the choices of gauge and resummations. To get a more direct measure of the impact of including the conservative 1GSF corrections to the Hamiltonian, we also consider a version of SEOBNR-GSF in which we have turned these corrections off by setting $Z_{\rm fit}$ in Eq. (27) to 0, replacing $Z_{\rm PN}$ by its 21.5 PN truncation, and recalibrating $\Delta t_{\rm NR}$. This version will be labeled "SEOBNR-GSF-PN with $\Delta t_{\rm NR}$" in the following.

In Fig. 8, we plot the distribution of the maximum mismatch for the three models, with the medians of the mismatch distributions highlighted by the vertical dashed lines. The median of SEOBNR-GSF, $\mathcal{M}_{\rm median} \sim 6.6 \times 10^{-4}$, falls just above that of SEOBNRV5, which in itself represents remarkably good agreement. SEOBNR-GSF-PN, on the other hand, has a median value of $\mathcal{M}_{\rm median} \sim 3.7 \times 10^{-3}$, which is an order of magnitude worse than SEOBNRV5 and performs significantly worse than SEOBNR-GSF over the full range of binary's total mass. Figure 8 also emphasizes the exceptional agreement of SEOBNRV5 in the nonspinning case, which was also highlighted in Refs. [50,52].

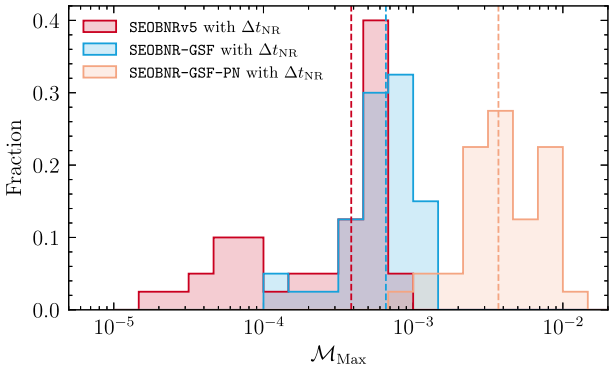


FIG. 8. Plot of the distribution of the maximum mismatch, $\mathcal{M}_{\rm Max}$, for the calibrated models we have presented in this work: SEOBNR-GSF, SEOBNRV5 and SEOBNR-GSF-PN. This comparison was done with a public subset of nonspinning, circular SXS NR waveforms over the binary's total mass range from $10M_\odot \leq M \leq 300M_\odot$. The vertical dashed lines indicate the medians of the maximum mismatch. Here we highlight the similar distributions and mismatch of the SEOBNR-GSF, SEOBNRV5, but also emphasize the major improvement the inclusion the fit of GSF data has on the mismatch by comparing the distributions of SEOBNR-GSF and SEOBNR-GSF-PN.

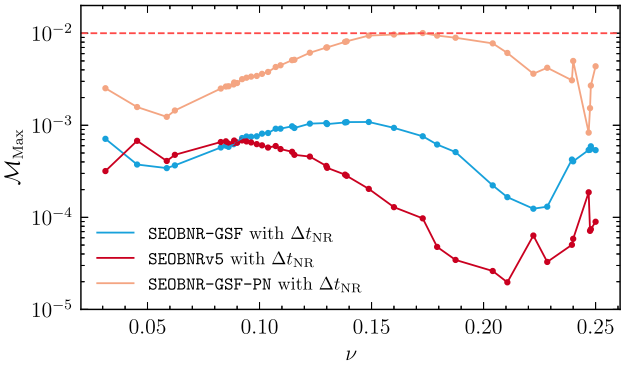


FIG. 9. Comparison of maximum mismatch, $\mathcal{M}_{\rm Max}$, as a function of mass ratio, ν, for the public subset of nonspinning, circular SXS NR waveforms, comparing the different calibrated models we have presented in this work: SEOBNR-GSF, SEOBNRV5, and SEOBNR-GSF-PN. For low mass-ratios, $\mathcal{M}_{\rm Max}$ of SEOBNR-GSF is comparable to that of SEOBNRV5, but shows a decline in performance for more comparable masses. Nevertheless, this underperformance remains significantly better than that of SEOBNR-GSF-PN, where $\mathcal{M}_{\rm Max}$ increases dramatically with rising ν, underscoring the importance of including GSF data.

The main question emanating from Fig. 8 is whether the SEOBNR-GSF model is performing less well than SEOBNRV5 broadly across the range of simulations, or whether there is a specific region of parameter space for which SEOBNR-GSF underperforms compared to SEOBNRV5. We find that the maximum mismatch degrades for more comparable mass ratios for SEOBNR-GSF. This is illustrated in Fig. 9, which plots the maximum mismatch, $\mathcal{M}_{\rm Max}$, against the mass ratio, ν, for both models. One observes that the improvement in maximum mismatch of SEOBNR-GSF relative to SEOBNR-GSF-PN steadily grows with symmetric mass-ratio ν, as one would expect from a higher order in ν correction. On the other hand, the perfomance of SEOBNR-GSF relative to SEOBNRV5 is comparable for $\nu \lesssim 0.10$, but for increasing $\nu \to 0.25$ the difference between the mismatches of the two models worsens. In this region, the tuning of $\Delta t_{\rm NR}$ for SEOBNR-GSF degrades. This was exemplified in Sec. V A, as the calibration was hampered at these mass ratios by issues of multimodality.

A key distinction between SEOBNRV5 and SEOBNR-GSF lies in the inclusion of the Padé resummation of the Hamiltonian based on Taylor-expanded PN information. This resummation allows greater flexibility in the calibration parameters, particularly $\Delta t_{\rm NR}$, which in turn improves agreement with NR. SEOBNR-GSF lacks such resummation in the Hamiltonian. Moreover, the PS gauge appears to be a suboptimal choice, despite resolving the LR divergence issue. This is evident in the EOB model dynamics, which show that in this specific gauge, the Hamiltonian remains too close to the probe limit ($\nu \to 0$) in the strong-field regime, as highlighted in Ref. [84]. Consequently, it lacks the flexibility afforded by the resummed SEOBNRV5 Hamiltonian. Our investigations further underscore the importance of resummation techniques, showing that without resumming the potentials in the SEOBNRV5 Hamiltonian, the model's posteriors are too weakly constrained to permit meaningful calibration of $\Delta t_{\rm NR}$.

VII. SUMMARY AND DISCUSSION

In this paper we have constructed a full (quasicircular) inspiral-merger-ringdown EOB model, SEOBNR-GSF, that for its inspiral dynamics takes inputs only from GSF and PN results without any calibration to NR results in the EOB Hamiltonian and radiation-reaction force. Calibration to NR for this model happens for the merger and ringdown phase in the form of NQC corrections and calibration of the attachment time $\Delta t_{\rm NR}$. For the inspiral phase we include both 1GSF conservative corrections following Ref. [84] and 2GSF dissipative results following Ref. [52]. Consequently, the model should nominally achieve 1PA accuracy.

A central objective of this study was to assess the performance of SEOBNR-GSF model relative to alternative approaches, including the SEOBNRV5 model and direct GSF calculations, particularly the 1PAT1 model. The most significant improvements in our model arise from the integration of GSF-based corrections, especially at lower mass ratios, where the dephasing between SEOBNR-GSF and NR waveforms remains small across the inspiral and early plunge phases. For low mass-ratio systems, SEOBNR-GSF exhibits phase differences of less than 0.1 radians up to $900M$ before merger, which is comparable to SEOBNRV5.

An further noteworthy aspect of this study was the comparison between SEOBNR-GSF and direct GSF models, such as the 1PAT1 variant. As expected, 1PAT1 performs well in the early inspiral but begins to deviate substantially from NR as the binary approaches the ISCO. The multiscale expansion inherent in the 1PAT1 model leads to divergences that render it unreliable near ISCO, whereas the SEOBNR-GSF model, which does not rely on these approximations, continues to produce valid waveforms through the merger phase. This reinforces the benefit of adopting the EOB formalism, which naturally accommodates the entire coalescence process, as opposed to a purely GSF approach with a multiscale expansion of the 1PAT1 model, which is limited to the inspiral.

While SEOBNR-GSF remains reliable during the inspiral for a wide range of mass ratios, it performs less well during the late plunge and merger phases, particularly in the comparable-mass regime where $q \lesssim 1/5$, where phase discrepancies grow more pronounced. This degradation is largely due to the absence of a resummed Hamiltonian and the use of the PS-gauge, both of which limit the model's fidelity in the strong-field regime. By contrast, SEOBNRV5 benefits from more sophisticated resummation techniques that allow the model to better capture the late-time dynamics. These differences highlight current limitations in the SEOBNR-GSF framework and motivate the need for further development.

A key feature of our approach was the minimal calibration effort required for SEOBNR-GSF. Unlike SEOBNRV5, which includes multiple calibration parameters to improve agreement with NR data, our model primarily relied on a single calibration parameter, $\Delta t_{\rm NR}$, which was tuned using NR data. While this simplified calibration procedure yielded good results in the low mass-ratio regime, it may limit the model's flexibility when attempting to describe more complex systems, such as binaries with high-mass ratios or spinning components.

It is important to acknowledge that while SEOBNR-GSF shows promise, it does not yet match the overall accuracy of SEOBNRV5, particularly in the transition from inspiral to merger for higher mass ratios. One observation from our results is that the behavior of SEOBNR-GSF near merger becomes increasingly unnatural for mass-ratios $q \lesssim 1/5$ leading to a rapid deterioration of the mismatch with NR. The absence of a resummed Hamiltonian and the specific choice of PS gauge in SEOBNR-GSF lead to larger discrepancies in the strong-field regime. It will be important in follow-up work to examine alternative solutions.

Despite the limitations in terms of the choice of gauge and resummation, we show that the inclusion of the strong-field numerical GSF data into the Hamiltonian can offer substantial improvements for full IMR EOB models. We demonstrate this by comparing the SEOBNR-GSF model to a version that does not include the strong-field data in the Hamiltonian, SEOBNR-GSF-PN. Postcalibration, SEOBNR-GSF improves the maximum mismatch by up to an order of magnitude, strongly suggesting that further improvements may be possible with an alternative gauge choice.

There are several avenues for future improvement of the SEOBNR-GSF model. One of the most promising directions is the incorporation of spin effects, which are currently absent. Given the modular nature of the PYSEOBNR framework, incorporating spin is a natural next step. Additionally, exploring alternative gauge choices and resummation techniques may further enhance the model's performance, particularly in the comparable-mass regime.

ACKNOWLEDGMENTS

The authors would like thank to Lorenzo Pompilli and Mohammed Khalil for their insightful discussions, which greatly contributed to the completion of this work. They also thank Raffi Enficiaud for his invaluable assistance with scientific computing. The authors are also grateful to members of the Multiscale Self-Force (MSF) collaboration: Barry Wardell, Niels Warburton, and Adam Pound, for providing the new 2GSF data utilized in this work. M. vdM. acknowledges financial support by the VILLUM Foundation (Grant No. VIL37766), the DNRF Chair program (Grant No. DNRF162) by the Danish National Research Foundation, and the European Union's Horizon ERC Synergy Grant "Making Sense of the Unexpected in the Gravitational-Wave Sky" Grant Agreement No. GWSky–101167314.

Views and opinions expressed are however those of the authors only and do not necessarily reflect those of the European Union or the European Research Council. Neither the European Union nor the granting authority can be held responsible for them.

DATA AVAILABILITY

The data are not publicly available. The data are available from the authors upon reasonable request.

APPENDIX A: SOLUTIONS TO HAMILTON'S EQUATIONS

In this section we briefly reproduce the intermediate solutions of the two Hamilton's equations used in the construction of the post-Schwarzschild gauge Hamiltonian potential, $\hat{Q}^{\rm PS}_{\rm SF}$-potential, in Sec. III. These solutions were previously reported by Antonelli *et al.* in Ref. [84], but are presented here for completeness.

First, the solution for the mass-reduced circular-orbit angular momentum, $\hat{p}^{\rm circ}_{\varphi}$, to Eq. (20), is given by

$$\begin{aligned}\hat{p}^{\rm circ}_{\varphi}(u,\nu) = {}& \frac{1}{\sqrt{u(1-3u)}} + \nu\frac{(1-2u)^2}{4(1-3u)^3\sqrt{u}}[2(1-2u)^3 f_0(u) + 2(1-3u)^{3/2} f_1(u) + 2(1-2u)(1-3u) f_2(u)\ln E_S^{-2}(u) \\ & - (1-2u)^4 f_0'(u) - (1-2u)(1-3u)^{3/2} f_1'(u) - (1-2u)^2(1-3u)\ln E_S^{-2}(u) f_2'(u)] + \mathcal{O}(\nu^2), \end{aligned} \tag{A1}$$

up to linear order in ν, where $f_i'(u) \coloneqq df_i/du$.

The other intermediate expression, which is a solution to Eq. (21) after inserting Eq. (A1), is an expression of the (circular) inverse radius, u, in terms of the gauge invariant radius, x. One finds up to linear order in the mass ratio,

$$\begin{aligned} u^{\rm circ}(x,\nu) = {}& x + \frac{x\nu}{6(1-3x)^{3/2}}[4 - 20x + 24x^2 - (4-12x)\sqrt{1-3x} - 10(1-2x)^4 f_0(x) \\ & - 4\sqrt{1-3x}(1-5x+6x^2) f_1(x) + (4 - 28x + 64x^2 - 48x^3 - (6 - 42x + 96x^2 - 72x^3)\ln E^{-2}(x)) f_2(x) \\ & + (1 - 10x + 40x^2 - 80x^3 + 80x^4 - 32x^5) f_0'(x) + \sqrt{1-3x}(1 - 7x + 16x^2 - 12x^3) f_1'(x) \\ & + (1 - 9x + 30x^2 - 44x^3 + 24x^4)\ln E_S^{-2}(x) f_2'(x)] + \mathcal{O}(\nu^2). \end{aligned} \tag{A2}$$

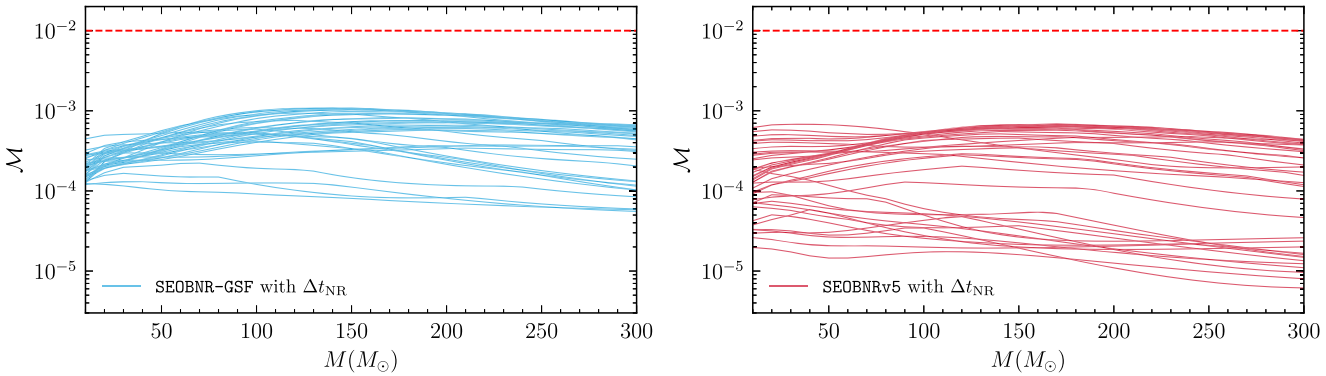


FIG. 10. Mismatches as a function of the total-mass of the binary, $10M_\odot \leq M \leq 300M_\odot$, for the two primary models featured in this work, SEOBNRV5 and SEOBNR-GSF, calibrated with the $\Delta t_{\rm NR}$ parameter. In this figure we use the complete set of nonspinning public SXS NR waveforms and we only consider the $(\ell, m) = (2, 2)$ mode.

APPENDIX B: MISMATCH COMPARISON

In this supplementary Appendix, we present Fig. 10, a complimentary figure to Fig. 9, that presents the mismatch of the $(\ell, m) = (2, 2)$ mode of SEOBNRV5 and SEOBNR-GSF as a function of the binary's total mass ranging over $10M_\odot$ to $300M_\odot$. This is in contrast to Figs. 8 and 9, which only present the maximum mismatch across the same range of total mass. As previously, the models here are only calibrated through the $\Delta t_{\rm NR}$ parameter.

APPENDIX C: NUMERICAL-RELATIVITY SIMULATIONS

In this work, we use a subset of publicly available NR simulations from the SXS collaboration [124,125] to calibrate and evaluate the performance of our EOB models. Table I lists the simulations employed, along with key reference parameters. Specifically, we utilize nonspinning, quasicircular binaries across a range of mass ratios.

TABLE I. A table summarizing the numerical relativity simulations from the SXS collaboration used in this work. The initial eccentricity is denoted by e, while χ_1 and χ_2 are the reference spins of the component black holes. The final column indicates the figures in which each simulation appears. Simulations used in the calibration procedure are indicated in italic.

ID	q	ν	e	χ_1	χ_2	Used in Fig.
SXS:BBH:2325	1.000	0.2500	7.86×10^{-5}	3.645×10^{-5}	3.602×10^{-5}	3–6, 8–10
SXS:BBH:0198	1.202	0.2479	2.04×10^{-4}	-5.042×10^{-5}	8.544×10^{-5}	4, 8–10
SXS:BBH:0310	1.221	0.2475	7.88×10^{-4}	1.456×10^{-4}	9.706×10^{-5}	4, 8–10
SXS:BBH:1143	1.250	0.2469	1.02×10^{-4}	-1.365×10^{-4}	-2.545×10^{-5}	4, 8–10
SXS:BBH:2331	1.500	0.2400	5.77×10^{-5}	-7.576×10^{-5}	-6.795×10^{-6}	3, 4, 8–10
SXS:BBH:0194	1.517	0.2394	8.02×10^{-4}	3.193×10^{-5}	-8.569×10^{-5}	4, 8–10
SXS:BBH:1354	1.832	0.2284	4.79×10^{-5}	-1.500×10^{-4}	1.264×10^{-4}	4, 8–10
SXS:BBH:2425	2.000	0.2222	2.89×10^{-4}	-7.663×10^{-5}	1.160×10^{-4}	2, 8–10
SXS:BBH:0201	2.316	0.2106	1.41×10^{-4}	6.266×10^{-5}	-4.156×10^{-5}	4, 8–10
SXS:BBH:0259	2.450	0.2041	4.90×10^{-4}	9.373×10^{-8}	2.478×10^{-7}	3, 4, 8–10
BFI:RerunCatalog_SHK:003	3.000	0.1875	9.64×10^{-5}	4.358×10^{-6}	3.132×10^{-6}	3, 8–10
SXS:BBH:0200	3.272	0.1792	4.14×10^{-4}	-5.023×10^{-5}	-1.095×10^{-5}	4, 8–10
SXS:BBH:0294	3.500	0.1728	4.34×10^{-5}	-2.312×10^{-7}	3.533×10^{-7}	3, 4, 8–10
SXS:BBH:2483	3.500	0.1728	2.67×10^{-4}	-2.705×10^{-5}	6.294×10^{-5}	4, 8–10
SXS:BBH:2499	4.000	0.1600	1.57×10^{-4}	8.406×10^{-5}	3.421×10^{-6}	4, 6, 8–10
BFI:RerunCatalog_SHK:004	4.000	0.1600	1.57×10^{-4}	8.406×10^{-6}	3.420×10^{-6}	3, 4, 8–10
BFI:q8_7d:0527	4.500	0.1488	2.36×10^{-4}	4.219×10^{-5}	2.865×10^{-5}	3, 4, 8–10
SXS:BBH:2374	5.000	0.1389	5.30×10^{-4}	-8.130×10^{-5}	5.244×10^{-5}	3, 4, 8–10
SXS:BBH:0187	5.039	0.1382	4.60×10^{-5}	8.798×10^{-6}	-1.204×10^{-5}	4, 5, 8–10
SXS:BBH:0296	5.500	0.1302	3.30×10^{-5}	2.513×10^{-7}	3.072×10^{-7}	3, 4, 8–10
SXS:BBH:2486	5.500	0.1302	4.44×10^{-4}	2.801×10^{-6}	-9.807×10^{-6}	4, 8–10

(Table continued)

TABLE I. *(Continued)*

ID	q	ν	e	χ_1	χ_2	Used in Fig.
SXS:BBH:0197	5.522	0.1298	2.20×10^{-4}	-3.702×10^{-5}	-1.524×10^{-5}	4, 8–10
SXS:BBH:2164	5.999	0.1225	3.85×10^{-4}	$-2,709 \times 10^{-6}$	-1.417×10^{-5}	3, 4, 8–10
SXS:BBH:0297	6.500	0.1155	5.29×10^{-5}	6.329×10^{-7}	5.524×10^{-7}	3, 4, 8–10
SXS:BBH:2488	6.500	0.1155	7.26×10^{-4}	2.792×10^{-5}	-2.407×10^{-5}	4, 8–10
SXS:BBH:0912	6.578	0.1145	5.02×10^{-5}	2.510×10^{-5}	-5.071×10^{-5}	4, 8–10
SXS:BBH:0298	7.000	0.1094	4.00×10^{-5}	6.904×10^{-7}	5.823×10^{-7}	3, 4, 8–10
SXS:BBH:2491	7.000	0.1094	3.61×10^{-4}	1.137×10^{-5}	4.506×10^{-5}	4, 8–10
SXS:BBH:0188	7.187	0.1072	1.61×10^{-4}	1.523×10^{-6}	-2.445×10^{-5}	4, 8–10
SXS:BBH:0299	7.500	0.1038	5.60×10^{-5}	7.131×10^{-7}	5.960×10^{-7}	3, 4, 8–10
SXS:BBH:2490	7.500	0.1038	5.52×10^{-4}	-2.915×10^{-5}	-5.938×10^{-6}	4, 8–10
SXS:BBH:0195	7.761	0.1011	2.24×10^{-4}	1.319×10^{-5}	-4.008×10^{-5}	4, 8–10
BFI:q8_7d:0086	8.000	0.09876	3.41×10^{-4}	-5.603×10^{-5}	6.588×10^{-5}	3, 4, 8–10
SXS:BBH:0186	8.267	0.09626	6.70×10^{-4}	1.017×10^{-6}	-8.824×10^{-8}	4, 8–10
SXS:BBH:0300	8.500	0.0942	6.00×10^{-5}	8.720×10^{-7}	7.241×10^{-7}	3, 4, 8–10
SXS:BBH:2492	8.501	0.09417	8.58×10^{-4}	-3.198×10^{-6}	-1.826×10^{-5}	4, 8–10
SXS:BBH:0199	8.729	0.09222	6.77×10^{-5}	-1.113×10^{-6}	-3.313×10^{-5}	4, 8–10
SXS:BBH:0301	9.000	0.0900	5.70×10^{-4}	8.874×10^{-7}	7.440×10^{-7}	3, 4, 8–10
SXS:BBH:2495	9.001	0.08999	2.01×10^{-4}	1.365×10^{-6}	-8.766×10^{-6}	4, 8–10
SXS:BBH:0189	9.167	0.08868	8.17×10^{-5}	1.183×10^{-5}	-6.788×10^{-6}	4, 8–10
SXS:BBH:1108	9.200	0.08843	1.48×10^{-4}	-2.253×10^{-6}	-1.464×10^{-6}	4, 8–10
SXS:BBH:2494	9.497	0.08619	1.59×10^{-4}	-1.568×10^{-5}	-3.539×10^{-5}	4, 8–10
SXS:BBH:0302	9.500	0.08617	5.40×10^{-4}	9.056×10^{-7}	7.641×10^{-7}	3, 4, 8–10
SXS:BBH:0196	9.663	0.08499	2.63×10^{-4}	1.673×10^{-6}	-2.731×10^{-5}	4, 8–10
SXS:BBH:0185	9.990	0.08272	2.93×10^{-4}	1.281×10^{-5}	-1.434×10^{-5}	3–5, 7–10
SXS:BBH:2480	14.00	0.06222	3.81×10^{-4}	7.625×10^{-6}	-4.136×10^{-6}	3, 4, 7–10
SXS:BBH:2477	15.00	0.05859	3.69×10^{-4}	6.433×10^{-6}	-4.521×10^{-6}	3, 4, 8–10
SXS:BBH:2325	20.00	0.04536	2.51×10^{-4}	3.434×10^{-5}	-1.022×10^{-4}	3, 4, 8–10

[1] B. P. Abbott *et al.* (LIGO Scientific Collaboration and Virgo Collaboration), Observation of gravitational waves from a binary black hole merger, Phys. Rev. Lett. **116**, 061102 (2016).

[2] F. Pretorius, Evolution of binary black hole spacetimes, Phys. Rev. Lett. **95**, 121101 (2005).

[3] J. G. Baker, J. Centrella, D.-I. Choi, M. Koppitz, and J. van Meter, Gravitational wave extraction from an inspiraling configuration of merging black holes, Phys. Rev. Lett. **96**, 111102 (2006).

[4] M. Campanelli, C. O. Lousto, P. Marronetti, and Y. Zlochower, Accurate evolutions of orbiting black-hole binaries without excision, Phys. Rev. Lett. **96**, 111101 (2006).

[5] T. Futamase and Y. Itoh, The post-Newtonian approximation for relativistic compact binaries, Living Rev. Relativity **10**, 2 (2007).

[6] L. Blanchet, Post-Newtonian theory for gravitational waves, Living Rev. Relativity **17**, 2 (2014).

[7] R. A. Porto, The effective field theorist's approach to gravitational dynamics, Phys. Rep. **633**, 1 (2016).

[8] G. Schäfer and P. Jaranowski, Hamiltonian formulation of general relativity and post-Newtonian dynamics of compact binaries, Living Rev. Relativity **21**, 7 (2018).

[9] M. Levi, Effective field theories of post-Newtonian gravity: A comprehensive review, Rep. Prog. Phys. **83**, 075901 (2020).

[10] P. Jaranowski and G. Schaefer, Third post-Newtonian higher order ADM Hamilton dynamics for two-body point mass systems, Phys. Rev. D **57**, 7274 (1998); **63**, 029902 (E) (2001).

[11] T. Damour, P. Jaranowski, and G. Schäfer, Nonlocal-in-time action for the fourth post-Newtonian conservative dynamics of two-body systems, Phys. Rev. D **89**, 064058 (2014).

[12] P. Jaranowski and G. Schäfer, Derivation of local-in-time fourth post-Newtonian ADM Hamiltonian for spinless compact binaries, Phys. Rev. D **92**, 124043 (2015).

[13] L. Bernard, L. Blanchet, A. Bohé, G. Faye, and S. Marsat, Fokker action of nonspinning compact binaries at the fourth post-Newtonian approximation, Phys. Rev. D **93**, 084037 (2016).
[14] L. Bernard, L. Blanchet, A. Bohé, G. Faye, and S. Marsat, Energy and periastron advance of compact binaries on circular orbits at the fourth post-Newtonian order, Phys. Rev. D **95**, 044026 (2017).
[15] T. Damour, P. Jaranowski, and G. Schäfer, Conservative dynamics of two-body systems at the fourth post-Newtonian approximation of general relativity, Phys. Rev. D **93**, 084014 (2016).
[16] L. Blanchet, G. Faye, Q. Henry, F. Larrouturou, and D. Trestini, Gravitational-wave flux and quadrupole modes from quasicircular nonspinning compact binaries to the fourth post-Newtonian order, Phys. Rev. D **108**, 064041 (2023).
[17] L. Blanchet, G. Faye, Q. Henry, F. Larrouturou, and D. Trestini, Gravitational-wave phasing of quasicircular compact binary systems to the fourth-and-a-half post-Newtonian order, Phys. Rev. Lett. **131**, 121402 (2023).
[18] K. Westpfahl and M. Goller, Gravitational scattering of two relativistic particles in postlinear approximation, Lett. Nuovo Cimento **26**, 573 (1979).
[19] K. Westpfahl and H. Hoyler, Gravitational Bremsstrahlung in postlinear fast motion approximation, Lett. Nuovo Cimento **27**, 581 (1980).
[20] L. Bel, T. Damour, N. Deruelle, J. Ibanez, and J. Martin, Poincaré-invariant gravitational field and equations of motion of two pointlike objects: The postlinear approximation of general relativity, Gen. Relativ. Gravit. **13**, 963 (1981).
[21] K. Westpfahl, High-speed scattering of charged and uncharged particles in general relativity, Fortschr. Phys. **33**, 417 (1985).
[22] T. Ledvinka, G. Schaefer, and J. Bicak, Relativistic closed-form Hamiltonian for many-body gravitating systems in the post-Minkowskian approximation, Phys. Rev. Lett. **100**, 251101 (2008).
[23] A. Buonanno, M. Khalil, D. O'Connell, R. Roiban, M. P. Solon, and M. Zeng, Snowmass white paper: Gravitational waves and scattering amplitudes, in *Snowmass 2021* (2022), https://inspirehep.net/literature/2065377.
[24] G. Travaglini *et al.*, The SAGEX review on scattering amplitudes, J. Phys. A **55**, 443001 (2022).
[25] N. E. J. Bjerrum-Bohr, P. H. Damgaard, L. Plante, and P. Vanhove, The SAGEX review on scattering amplitudes Chapter 13: Post-Minkowskian expansion from scattering amplitudes, J. Phys. A **55**, 443014 (2022).
[26] D. A. Kosower, R. Monteiro, and D. O'Connell, The SAGEX review on scattering amplitudes Chapter 14: Classical gravity from scattering amplitudes, J. Phys. A **55**, 443015 (2022).
[27] J. Blackman, S. E. Field, C. R. Galley, B. Szilágyi, M. A. Scheel, M. Tiglio, and D. A. Hemberger, Fast and accurate prediction of numerical relativity waveforms from binary black hole coalescences using surrogate models, Phys. Rev. Lett. **115**, 121102 (2015).
[28] J. Blackman, S. E. Field, M. A. Scheel, C. R. Galley, D. A. Hemberger, P. Schmidt, and R. Smith, A surrogate model of gravitational waveforms from numerical relativity simulations of precessing binary black hole mergers, Phys. Rev. D **95**, 104023 (2017).
[29] J. Blackman, S. E. Field, M. A. Scheel, C. R. Galley, C. D. Ott, M. Boyle, L. E. Kidder, H. P. Pfeiffer, and B. Szilágyi, Numerical relativity waveform surrogate model for generically precessing binary black hole mergers, Phys. Rev. D **96**, 024058 (2017).
[30] V. Varma, S. E. Field, M. A. Scheel, J. Blackman, L. E. Kidder, and H. P. Pfeiffer, Surrogate model of hybridized numerical relativity binary black hole waveforms, Phys. Rev. D **99**, 064045 (2019).
[31] V. Varma, S. E. Field, M. A. Scheel, J. Blackman, D. Gerosa, L. C. Stein, L. E. Kidder, and H. P. Pfeiffer, Surrogate models for precessing binary black hole simulations with unequal masses, Phys. Rev. Res. **1**, 033015 (2019).
[32] D. Williams, I. S. Heng, J. Gair, J. A. Clark, and B. Khamesra, Precessing numerical relativity waveform surrogate model for binary black holes: A Gaussian process regression approach, Phys. Rev. D **101**, 063011 (2020).
[33] N. E. M. Rifat, S. E. Field, G. Khanna, and V. Varma, Surrogate model for gravitational wave signals from comparable and large-mass-ratio black hole binaries, Phys. Rev. D **101**, 081502 (2020).
[34] Y. Pan, A. Buonanno, J. G. Baker, J. Centrella, B. J. Kelly, S. T. McWilliams, F. Pretorius, and J. R. van Meter, A Data-analysis driven comparison of analytic and numerical coalescing binary waveforms: Nonspinning case, Phys. Rev. D **77**, 024014 (2008).
[35] P. Ajith *et al.*, Phenomenological template family for black-hole coalescence waveforms, Classical Quantum Gravity **24**, S689 (2007).
[36] P. Ajith *et al.*, Inspiral-merger-ringdown waveforms for black-hole binaries with non-precessing spins, Phys. Rev. Lett. **106**, 241101 (2011).
[37] L. Santamaria *et al.*, Matching post-Newtonian and numerical relativity waveforms: Systematic errors and a new phenomenological model for non-precessing black hole binaries, Phys. Rev. D **82**, 064016 (2010).
[38] M. Hannam, P. Schmidt, A. Bohé, L. Haegel, S. Husa, F. Ohme, G. Pratten, and M. Pürrer, Simple model of complete precessing black-hole-binary gravitational waveforms, Phys. Rev. Lett. **113**, 151101 (2014).
[39] S. Husa, S. Khan, M. Hannam, M. Pürrer, F. Ohme, X. Jiménez Forteza, and A. Bohé, Frequency-domain gravitational waves from nonprecessing black-hole binaries. I. New numerical waveforms and anatomy of the signal, Phys. Rev. D **93**, 044006 (2016).
[40] S. Khan, S. Husa, M. Hannam, F. Ohme, M. Pürrer, X. Jiménez Forteza, and A. Bohé, Frequency-domain gravitational waves from nonprecessing black-hole binaries. II. A phenomenological model for the advanced detector era, Phys. Rev. D **93**, 044007 (2016).
[41] L. London, S. Khan, E. Fauchon-Jones, C. García, M. Hannam, S. Husa, X. Jiménez-Forteza, C. Kalaghatgi, F. Ohme, and F. Pannarale, First higher-multipole model of gravitational waves from spinning and coalescing black-hole binaries, Phys. Rev. Lett. **120**, 161102 (2018).

[42] S. Khan, K. Chatziioannou, M. Hannam, and F. Ohme, Phenomenological model for the gravitational-wave signal from precessing binary black holes with two-spin effects, Phys. Rev. D **100**, 024059 (2019).
[43] S. Khan, F. Ohme, K. Chatziioannou, and M. Hannam, Including higher order multipoles in gravitational-wave models for precessing binary black holes, Phys. Rev. D **101**, 024056 (2020).
[44] A. Buonanno and T. Damour, Effective one-body approach to general relativistic two-body dynamics, Phys. Rev. D **59**, 084006 (1999).
[45] A. Buonanno and T. Damour, Transition from inspiral to plunge in binary black hole coalescences, Phys. Rev. D **62**, 064015 (2000).
[46] T. Damour, P. Jaranowski, and G. Schaefer, On the determination of the last stable orbit for circular general relativistic binaries at the third postNewtonian approximation, Phys. Rev. D **62**, 084011 (2000).
[47] T. Damour, Coalescence of two spinning black holes: An effective one-body approach, Phys. Rev. D **64**, 124013 (2001).
[48] A. Buonanno, Y. Chen, and T. Damour, Transition from inspiral to plunge in precessing binaries of spinning black holes, Phys. Rev. D **74**, 104005 (2006).
[49] A. Buonanno, G. B. Cook, and F. Pretorius, Inspiral, merger and ring-down of equal-mass black-hole binaries, Phys. Rev. D **75**, 124018 (2007).
[50] L. Pompili *et al.*, Laying the foundation of the effective-one-body waveform models `SEOBNRV5`: Improved accuracy and efficiency for spinning nonprecessing binary black holes, Phys. Rev. D **108**, 124035 (2023).
[51] A. Ramos-Buades, A. Buonanno, H. Estellés, M. Khalil, D. P. Mihaylov, S. Ossokine, L. Pompili, and M. Shiferaw, Next generation of accurate and efficient multipolar precessing-spin effective-one-body waveforms for binary black holes, Phys. Rev. D **108**, 124037 (2023).
[52] M. van de Meent, A. Buonanno, D. P. Mihaylov, S. Ossokine, L. Pompili, N. Warburton, A. Pound, B. Wardell, L. Durkan, and J. Miller, Enhancing the `SEOBNRV5` effective-one-body waveform model with second-order gravitational self-force fluxes, Phys. Rev. D **108**, 124038 (2023).
[53] M. Khalil, A. Buonanno, H. Estelles, D. P. Mihaylov, S. Ossokine, L. Pompili, and A. Ramos-Buades, Theoretical groundwork supporting the precessing-spin two-body dynamics of the effective-one-body waveform models `SEOBNRV5`, Phys. Rev. D **108**, 124036 (2023).
[54] A. Ramos-Buades, A. Buonanno, M. Khalil, and S. Ossokine, Effective-one-body multipolar waveforms for eccentric binary black holes with nonprecessing spins, Phys. Rev. D **105**, 044035 (2022).
[55] A. Nagar *et al.*, Time-domain effective-one-body gravitational waveforms for coalescing compact binaries with nonprecessing spins, tides and self-spin effects, Phys. Rev. D **98**, 104052 (2018).
[56] A. Nagar, G. Pratten, G. Riemenschneider, and R. Gamba, Multipolar effective one body model for nonspinning black hole binaries, Phys. Rev. D **101**, 024041 (2020).
[57] A. Nagar, G. Riemenschneider, G. Pratten, P. Rettegno, and F. Messina, Multipolar effective one body waveform model for spin-aligned black hole binaries, Phys. Rev. D **102**, 024077 (2020).
[58] R. Gamba, S. Akçay, S. Bernuzzi, and J. Williams, Effective-one-body waveforms for precessing coalescing compact binaries with post-Newtonian twist, Phys. Rev. D **106**, 024020 (2022).
[59] A. Nagar, P. Rettegno, R. Gamba, S. Albanesi, A. Albertini, and S. Bernuzzi, Analytic systematics in next generation of effective-one-body gravitational waveform models for future observations, Phys. Rev. D **108**, 124018 (2023).
[60] B. P. Abbott *et al.* (LIGO Scientific Collaboration), LIGO: The Laser interferometer gravitational-wave observatory, Rep. Prog. Phys. **72**, 076901 (2009).
[61] J. Aasi *et al.* (LIGO Scientific Collaboration), Advanced LIGO, Classical Quantum Gravity **32**, 074001 (2015).
[62] J. Aasi *et al.* (LIGO Scientific Collaboration and VIRGO Collaboration), Characterization of the LIGO detectors during their sixth science run, Classical Quantum Gravity **32**, 115012 (2015).
[63] A. Buikema *et al.*, Sensitivity and performance of the advanced ligo detectors in the third observing run, Phys. Rev. D **102**, 062003 (2020).
[64] M. Tse *et al.*, Quantum-enhanced advanced LIGO detectors in the era of gravitational-wave astronomy, Phys. Rev. Lett. **123**, 231107 (2019).
[65] T. Accadia *et al.* (VIRGO Collaboration), Virgo: A laser interferometer to detect gravitational waves, J. Instrum. **7**, P03012 (2012).
[66] F. Acernese *et al.* (VIRGO Collaboration), Advanced Virgo: A second-generation interferometric gravitational wave detector, Classical Quantum Gravity **32**, 024001 (2015).
[67] F. Acernese *et al.* (Virgo Collaboration), Increasing the astrophysical reach of the advanced virgo detector via the application of squeezed vacuum states of light, Phys. Rev. Lett. **123**, 231108 (2019).
[68] T. Akutsu *et al.*, Overview of KAGRA: Detector design and construction history, Prog. Theor. Exp. Phys. **2021**, 05A101 (2020).
[69] Y. Aso, Y. Michimura, K. Somiya, M. Ando, O. Miyakawa, T. Sekiguchi, D. Tatsumi, and H. Yamamoto (KAGRA Collaboration), Interferometer design of the KAGRA gravitational wave detector, Phys. Rev. D **88**, 043007 (2013).
[70] K. Somiya (KAGRA Collaboration), Detector configuration of KAGRA: The Japanese cryogenic gravitational-wave detector, Classical Quantum Gravity **29**, 124007 (2012).
[71] M. Punturo *et al.*, The Einstein telescope: A third-generation gravitational wave observatory, Classical Quantum Gravity **27**, 194002 (2010).
[72] D. Reitze *et al.*, Cosmic explorer: The U.S. contribution to gravitational-wave astronomy beyond LIGO, Bull. Am. Astron. Soc. **51**, 035 (2019), https://inspirehep.net/literature/1743201.
[73] M. Evans *et al.*, A horizon study for cosmic explorer: Science, observatories, and community, arXiv:2109.09882.

[74] P. Amaro-Seoane *et al.* (LISA Collaboration), Laser interferometer space antenna, arXiv:1702.00786.
[75] S. Borhanian and B. S. Sathyaprakash, Listening to the universe with next generation ground-based gravitational-wave detectors, Phys. Rev. D **110**, 083040 (2024).
[76] M. Pürrer and C.-J. Haster, Gravitational waveform accuracy requirements for future ground-based detectors, Phys. Rev. Res. **2**, 023151 (2020).
[77] A. Dhani, S. Völkel, A. Buonanno, H. Estelles, J. Gair, H. P. Pfeiffer, L. Pompili, and A. Toubiana, Systematic biases in estimating the properties of black holes due to inaccurate gravitational-wave models, arXiv:2404.05811.
[78] A. Buonanno, G. Mogull, R. Patil, and L. Pompili, Post-Minkowskian Theory meets the spinning effective-one-body approach for bound-orbit waveforms, Phys. Rev. Lett. **133**, 211402 (2024).
[79] N. Warburton, A. Pound, B. Wardell, J. Miller, and L. Durkan, Gravitational-wave energy flux for compact binaries through second order in the mass ratio, Phys. Rev. Lett. **127**, 151102 (2021).
[80] A. Pound, B. Wardell, N. Warburton, and J. Miller, Second-order self-force calculation of gravitational binding energy in compact binaries, Phys. Rev. Lett. **124**, 021101 (2020).
[81] B. Wardell, A. Pound, N. Warburton, J. Miller, L. Durkan, and A. Le Tiec, Gravitational waveforms for compact binaries from second-order self-force theory, Phys. Rev. Lett. **130**, 241402 (2023).
[82] L. Barack and N. Sago, Gravitational self-force correction to the innermost stable circular orbit of a Schwarzschild black hole, Phys. Rev. Lett. **102**, 191101 (2009).
[83] S. Akcay, L. Barack, T. Damour, and N. Sago, Gravitational self-force and the effective-one-body formalism between the innermost stable circular orbit and the light ring, Phys. Rev. D **86**, 104041 (2012).
[84] A. Antonelli, M. van de Meent, A. Buonanno, J. Steinhoff, and J. Vines, Quasicircular inspirals and plunges from nonspinning effective-one-body Hamiltonians with gravitational self-force information, Phys. Rev. D **101**, 024024 (2020).
[85] T. Damour, High-energy gravitational scattering and the general relativistic two-body problem, Phys. Rev. D **97**, 044038 (2018).
[86] D. Bini, T. Damour, and A. Geralico, Binary dynamics at the fifth and fifth-and-a-half post-Newtonian orders, Phys. Rev. D **102**, 024062 (2020).
[87] A. Buonanno, Y. Pan, J. G. Baker, J. Centrella, B. J. Kelly, S. T. McWilliams, and J. R. van Meter, Toward faithful templates for non-spinning binary black holes using the effective-one-body approach, Phys. Rev. D **76**, 104049 (2007).
[88] T. Damour, B. R. Iyer, P. Jaranowski, and B. S. Sathyaprakash, Gravitational waves from black hole binary inspiral and merger: The span of third postNewtonian effective one-body templates, Phys. Rev. D **67**, 064028 (2003).
[89] S. L. Detweiler, A consequence of the gravitational self-force for circular orbits of the Schwarzschild geometry, Phys. Rev. D **77**, 124026 (2008).
[90] L. Barack and N. Sago, Gravitational self-force on a particle in eccentric orbit around a Schwarzschild black hole, Phys. Rev. D **81**, 084021 (2010).
[91] E. Barausse, A. Buonanno, and A. Le Tiec, The complete non-spinning effective-one-body metric at linear order in the mass ratio, Phys. Rev. D **85**, 064010 (2012).
[92] A. Le Tiec, E. Barausse, and A. Buonanno, Gravitational self-force correction to the binding energy of compact binary systems, Phys. Rev. Lett. **108**, 131103 (2012).
[93] D. Bini and T. Damour, Gravitational self-force corrections to two-body tidal interactions and the effective one-body formalism, Phys. Rev. D **90**, 124037 (2014).
[94] S. R. Dolan, P. Nolan, A. C. Ottewill, N. Warburton, and B. Wardell, Tidal invariants for compact binaries on quasi-circular orbits, Phys. Rev. D **91**, 023009 (2015).
[95] C. Kavanagh, A. C. Ottewill, and B. Wardell, Analytical high-order post-Newtonian expansions for extreme mass ratio binaries, Phys. Rev. D **92**, 084025 (2015).
[96] A. Pound, Self-force effects on the horizon geometry of a small black hole (2015).
[97] A. Zimmerman, A. G. M. Lewis, and H. P. Pfeiffer, Redshift factor and the first law of binary black hole mechanics in numerical simulations, Phys. Rev. Lett. **117**, 191101 (2016).
[98] A. Le Tiec, L. Blanchet, and B. F. Whiting, The first law of binary black hole mechanics in general relativity and post-Newtonian theory, Phys. Rev. D **85**, 064039 (2012).
[99] D. Bini and T. Damour, Conservative second-order gravitational self-force on circular orbits and the effective one-body formalism, Phys. Rev. D **93**, 104040 (2016).
[100] A. Antonelli, A. Buonanno, J. Steinhoff, M. van de Meent, and J. Vines, Energetics of two-body Hamiltonians in post-Minkowskian gravity, Phys. Rev. D **99**, 104004 (2019).
[101] T. Damour, P. Jaranowski, and G. Schäfer, Fourth post-Newtonian effective one-body dynamics, Phys. Rev. D **91**, 084024 (2015).
[102] M. van de Meent and A. G. Shah, Metric perturbations produced by eccentric equatorial orbits around a Kerr black hole, Phys. Rev. D **92**, 064025 (2015).
[103] C. Kavanagh, A. C. Ottewill, and B. Wardell, Analytical high-order post-Newtonian expansions for spinning extreme mass ratio binaries, Phys. Rev. D **93**, 124038 (2016).
[104] LVK Observing Run Plans, https://observing.docs.ligo.org/plan/.
[105] D. P. Mihaylov, S. Ossokine, A. Buonanno, H. Estelles, L. Pompili, M. Pürrer, and A. Ramos-Buades, PYSEOBNR: A software package for the next generation of effective-one-body multipolar waveform models, arXiv:2303.18203.
[106] J. M. Bardeen, W. H. Press, and S. A. Teukolsky, Rotating black holes: Locally nonrotating frames, energy extraction, and scalar synchrotron radiation, Astrophys. J. **178**, 347 (1972).
[107] R. Cotesta, A. Buonanno, A. Bohé, A. Taracchini, I. Hinder, and S. Ossokine, Enriching the symphony of gravitational waves from binary black holes by tuning higher harmonics, Phys. Rev. D **98**, 084028 (2018).
[108] T. Damour, A. Nagar, M. Hannam, S. Husa, and B. Bruegmann, Accurate effective-one-body waveforms of inspiralling and coalescing black-hole binaries, Phys. Rev. D **78**, 044039 (2008).

[109] A. Buonanno, Y. Pan, H. P. Pfeiffer, M. A. Scheel, L. T. Buchman, and L. E. Kidder, Effective-one-body waveforms calibrated to numerical relativity simulations: Coalescence of non-spinning, equal-mass black holes, Phys. Rev. D **79**, 124028 (2009).
[110] T. Damour and A. Nagar, Faithful effective-one-body waveforms of small-mass-ratio coalescing black-hole binaries, Phys. Rev. D **76**, 064028 (2007).
[111] T. Damour and A. Nagar, Comparing effective-one-body gravitational waveforms to accurate numerical data, Phys. Rev. D **77**, 024043 (2008).
[112] T. Damour, B. R. Iyer, and A. Nagar, Improved resummation of post-Newtonian multipolar waveforms from circularized compact binaries, Phys. Rev. D **79**, 064004 (2009).
[113] Y. Pan, A. Buonanno, R. Fujita, E. Racine, and H. Tagoshi, Post-Newtonian factorized multipolar waveforms for spinning, non-precessing black-hole binaries, Phys. Rev. D **83**, 064003 (2011); **87**, 109901(E) (2013).
[114] L. Blanchet, Gravitational wave tails of tails, Classical Quantum Gravity **15**, 113 (1998); **22**, 3381(E) (2005).
[115] A. Nagar and S. Akcay, Horizon-absorbed energy flux in circularized, nonspinning black-hole binaries and its effective-one-body representation, Phys. Rev. D **85**, 044025 (2012).
[116] A. Nagar and S. Albanesi, Toward a gravitational self-force-informed effective-one-body waveform model for nonprecessing, eccentric, large-mass-ratio inspirals, Phys. Rev. D **106**, 064049 (2022).
[117] T. Damour and A. Nagar, A new analytic representation of the ringdown waveform of coalescing spinning black hole binaries, Phys. Rev. D **90**, 024054 (2014).
[118] A. Bohé *et al.*, Improved effective-one-body model of spinning, nonprecessing binary black holes for the era of gravitational-wave astrophysics with advanced detectors, Phys. Rev. D **95**, 044028 (2017).
[119] E. Barausse, A. Buonanno, S. A. Hughes, G. Khanna, S. O'Sullivan, and Y. Pan, Modeling multipolar gravitational-wave emission from small mass-ratio mergers, Phys. Rev. D **85**, 024046 (2012).
[120] A. Taracchini, A. Buonanno, G. Khanna, and S. A. Hughes, Small mass plunging into a Kerr black hole: Anatomy of the inspiral-merger-ringdown waveforms, Phys. Rev. D **90**, 084025 (2014).
[121] Y. Pan, A. Buonanno, L. T. Buchman, T. Chu, L. E. Kidder, H. P. Pfeiffer, and M. A. Scheel, Effective-one-body waveforms calibrated to numerical relativity simulations: coalescence of non-precessing, spinning, equal-mass black holes, Phys. Rev. D **81**, 084041 (2010).
[122] X. Jiménez-Forteza, D. Keitel, S. Husa, M. Hannam, S. Khan, and M. Pürrer, Hierarchical data-driven approach to fitting numerical relativity data for nonprecessing binary black holes with an application to final spin and radiated energy, Phys. Rev. D **95**, 064024 (2017).
[123] F. Hofmann, E. Barausse, and L. Rezzolla, The final spin from binary black holes in quasi-circular orbits, Astrophys. J. Lett. **825**, L19 (2016).
[124] Sxs catalogue, http://www.black-holes.org/waveforms.
[125] M. Boyle *et al.*, The SXS Collaboration catalog of binary black hole simulations, Classical Quantum Gravity **36**, 195006 (2019).
[126] T. Chu, H. Fong, P. Kumar, H. P. Pfeiffer, M. Boyle, D. A. Hemberger, L. E. Kidder, M. A. Scheel, and B. Szilagyi, On the accuracy and precision of numerical waveforms: Effect of waveform extraction methodology, Classical Quantum Gravity **33**, 165001 (2016).
[127] D. A. Hemberger, G. Lovelace, T. J. Loredo, L. E. Kidder, M. A. Scheel, B. Szilágyi, N. W. Taylor, and S. A. Teukolsky, Final spin and radiated energy in numerical simulations of binary black holes with equal masses and equal, aligned or anti-aligned spins, Phys. Rev. D **88**, 064014 (2013).
[128] G. Lovelace *et al.*, Nearly extremal apparent horizons in simulations of merging black holes, Classical Quantum Gravity **32**, 065007 (2015).
[129] G. Lovelace *et al.*, Modeling the source of GW150914 with targeted numerical-relativity simulations, Classical Quantum Gravity **33**, 244002 (2016).
[130] A. H. Mroue *et al.*, Catalog of 174 binary black hole simulations for gravitational wave astronomy, Phys. Rev. Lett. **111**, 241104 (2013).
[131] J. Yoo, V. Varma, M. Giesler, M. A. Scheel, C.-J. Haster, H. P. Pfeiffer, L. E. Kidder, and M. Boyle, Targeted large mass ratio numerical relativity surrogate waveform model for GW190814, Phys. Rev. D **106**, 044001 (2022).
[132] L. S. Finn and D. F. Chernoff, Observing binary inspiral in gravitational radiation: One interferometer, Phys. Rev. D **47**, 2198 (1993).
[133] B. S. Sathyaprakash and S. V. Dhurandhar, Choice of filters for the detection of gravitational waves from coalescing binaries, Phys. Rev. D **44**, 3819 (1991).
[134] L. Barsotti, M. Fritschel, Peter an Evans, and S. Gras, Updated advanced LIGO sensitivity design curve (2018).
[135] A. Bohé, L. Shao, A. Taracchini, A. Buonanno, S. Babak, I. W. Harry, I. Hinder, S. Ossokine, M. Pürrer, V. Raymond, T. Chu, H. Fong, P. Kumar, H. P. Pfeiffer, M. Boyle, D. A. Hemberger, L. E. Kidder, G. Lovelace, M. A. Scheel, and B. Szilágyi, Improved effective-one-body model of spinning, nonprecessing binary black holes for the era of gravitational-wave astrophysics with advanced detectors, Phys. Rev. D **95**, 044028 (2017).
[136] R. Cotesta, A. Buonanno, A. Bohé, A. Taracchini, I. Hinder, and S. Ossokine, Enriching the symphony of gravitational waves from binary black holes by tuning higher harmonics, Phys. Rev. D **98**, 084028 (2018).
[137] F. Pedregosa, G. Varoquaux, A. Gramfort, V. Michel, B. Thirion, O. Grisel, M. Blondel, P. Prettenhofer, R. Weiss, V. Dubourg, J. Vanderplas, A. Passos, D. Cournapeau, M. Brucher, M. Perrot, and E. Duchesnay, Scikit-learn: Machine learning in PYTHON, J. Mach. Learn. Res. **12**, 2825 (2011).
[138] L. Küchler, G. Compère, L. Durkan, and A. Pound, Self-force framework for transition-to-plunge waveforms, SciPost Phys. **17**, 056 (2024).
[139] S. Isoyama, L. Barack, S. R. Dolan, A. Le Tiec, H. Nakano, A. G. Shah, T. Tanaka, and N. Warburton, Gravitational self-force correction to the innermost stable circular equatorial orbit of a Kerr black hole, Phys. Rev. Lett. **113**, 161101 (2014).

[140] S. Ossokine, T. Dietrich, E. Foley, R. Katebi, and G. Lovelace, Assessing the energetics of spinning binary black hole systems, Phys. Rev. D **98**, 104057 (2018).

[141] Y. Pan, A. Buonanno, M. Boyle, L. T. Buchman, L. E. Kidder, H. P. Pfeiffer, and M. A. Scheel, Inspiral-merger-ringdown multipolar waveforms of nonspinning black-hole binaries using the effective-one-body formalism, Phys. Rev. D **84**, 124052 (2011).

[142] A. Albertini, A. Nagar, A. Pound, N. Warburton, B. Wardell, L. Durkan, and J. Miller, Comparing second-order gravitational self-force, numerical relativity, and effective one body waveforms from inspiralling, quasicircular, and nonspinning black hole binaries, Phys. Rev. D **106**, 084061 (2022).

[143] L. Barack and N. Sago, Gravitational self force on a particle in circular orbit around a Schwarzschild black hole, Phys. Rev. D **75**, 064021 (2007).

[144] A. Pound, Self-consistent gravitational self-force, Phys. Rev. D **81**, 024023 (2010).

[145] A. Pound and J. Miller, Practical, covariant puncture for second-order self-force calculations, Phys. Rev. D **89**, 104020 (2014).

[146] A. Pound, Second-order perturbation theory: problems on large scales, Phys. Rev. D **92**, 104047 (2015).

[147] J. Miller and A. Pound, Two-timescale evolution of extreme-mass-ratio inspirals: Waveform generation scheme for quasicircular orbits in Schwarzschild spacetime, Phys. Rev. D **103**, 064048 (2021).

[148] J. Miller, B. Leather, A. Pound, and N. Warburton, Worldtube puncture scheme for first- and second-order self-force calculations in the Fourier domain, Phys. Rev. D **109**, 104010 (2024).

[149] B. Wardell and N. Warburton, Applying the effective-source approach to frequency-domain self-force calculations: Lorenz-gauge gravitational perturbations, Phys. Rev. D **92**, 084019 (2015).